

Using a multi-omics approach to identify novel therapeutics in multiple myeloma capable of overcoming drug resistance



Anna James-Bott

St Hilda's College

Nuffield Department of Orthopaedics,
Rheumatology and Musculoskeletal Sciences

University of Oxford

A thesis submitted for the degree of

Doctor of Philosophy

Michaelmas 2021

Acknowledgements

I would like to thank my supervisors Dr Adam Cribbs, Professor Udo Oppermann and Dr Sarah Gooding etc etc...

GSK... DTC... Family... Friends...

Abstract

Multiple myeloma (MM) is an incurable cancer of plasma cells, with an average five-year survival rate of approximately 50%. More novel therapeutics, namely proteasome inhibitors (PI) and immunomodulatory imide drugs, have almost doubled median survival time of MM patients. However, most patients relapse and become resistant to drugs they previously have been treated with. Acquired anti-cancer drug resistance remains one of the biggest barriers in the treatment of myeloma. Recently, epigenetic mechanisms have been implicated in both the onset of MM and in the development of drug resistance. This thesis aims to investigate the changes that drive proteasome inhibitor drug resistance and to identify epigenetic compounds capable of reversing the resistance phenotype, and characterise their mechanism of action.

Following an epigenetic compound library screen and bulk RNA-seq, a dual TRIM24/BRPF inhibitor (TRIM24i) was selected to be investigated further as it was shown to kill carfilzomib-resistant AMO-1 cells (aCFZ) in the presence of carfilzomib but had little effect on PI-sensitive (WT) AMO-1 cells, demonstrating that it is capable of re-sensitizing carfilzomib-resistant AMO-1 cells to carfilzomib. Transcriptomic, epigenomic and proteomic changes were studied using an array of ‘omic’ techniques, including bulk and single-cell RNA-Seq, phosphoproteomics, ubiquitinomics, total proteomics, CyTOF and ChIP-Seq (PROBABLY will at some point).

Contents

List of Figures	ix
List of Tables	x
List of Abbreviations	xi
1 Introduction	1
1.1 Overview	1
1.2 The adaptive immune system	1
1.2.1 Plasma cells	2
1.3 Multiple myeloma	3
1.3.1 Multiple myeloma cells	3
1.3.2 Epidemiology	3
1.3.3 Presentation	4
1.3.4 Treatment of multiple myeloma	5
1.3.5 Proteasome inhibitors	5
1.4 Drug resistance in multiple myeloma	7
1.5 Transcriptomics, proteomics and epigenomics	9
1.5.1 DNA and the genome	9
1.5.2 The epigenome	10
1.5.3 The transcriptome	11
1.5.4 The proteome	11
1.5.5 RNA-seq	11
1.5.6 ATAC-seq	13
1.5.7 Next generation sequencing	13
1.5.8 CyTOF	13
1.5.9 Liquid chromatography with tandem mass spectrometry	13
1.6 Summary	14
1.7 Aims	14

2 Aminoacyl tRNA synthetases and Halofuginone	15
2.1 Introduction	15
2.2 Function and structure of aminoacyl tRNA synthetases	16
2.2.1 Multi-tRNA synthetase complexes	18
2.3 aaRSs in disease	22
2.3.1 aaRSs in cancer	23
2.3.2 AIMPs in cancer	24
2.4 aaRSs as therapeutic targets	25
2.4.1 Parasites	25
2.4.2 Febrifugine and its derivatives	26
2.4.3 Halofuginone	26
2.4.4 The application of Halofuginone in cancer	29
2.5 Conclusion and future directions	32
3 Methods	33
3.1 Cell culture	33
3.1.1 AMO-1 cells	33
3.1.2 L363 cells	33
3.2 Compounds	34
3.2.1 Proteasome inhibitors	34
3.2.2 PRS inhibitors	34
3.2.3 Epigenetic inhibitors	34
3.3 Assays	35
3.3.1 Cell viability assays	35
3.3.2 Dose response curves	35
3.4 Bulk RNA-seq	36
3.4.1 RNA extraction	36
3.4.2 RNA library preparation	36
3.5 Single-cell RNA-seq	36
3.5.1 Cell encapsulation	36
3.5.2 Library preparation	37
3.6 ATAC-seq	37
3.6.1 Cell lysis	37
3.6.2 Transposition	38
3.6.3 DNA purification	38
3.6.4 PCR amplification	39
3.7 Pooling, denaturing and diluting libraries	39
3.8 Sequencing	39
3.9 Phosphoproteomics	39

3.9.1	Collecting cell pellets	39
3.9.2	Cell lysis	40
3.9.3	Protein quantification	40
3.9.4	Protein Digestion	40
3.9.5	Peptide purification	41
3.10	Ubiquitinomics	41
3.10.1	Collecting cell pellets	41
3.10.2	Cell lysis	41
3.10.3	Protein quantification	42
3.10.4	Protein digestion	42
3.10.5	Peptide purification	42
3.10.6	Immunoaffinity purification	43
3.11	Liquid-chromatography-tandem mass spectrometry	43
3.12	CyTOF	44
3.13	Data Processing	44
3.13.1	Bulk RNA-seq	44
3.13.2	ATAC-seq	44
3.13.3	Single-cell RNA-seq	45
3.13.4	LC-MS/MS	45
4	Computational workflow generation	46
4.1	Introduction	46
4.1.1	Reproducible workflows	46
4.1.2	Computational pipelines	47
4.2	scRNA-Seq pseudoalignment pipeline	47
4.2.1	Psuedoaligment	47
4.2.2	Benchmark	49
4.3	Updated scRNA-seq pipeline	55
4.4	scRNA-Seq velocity analysis pipeline	55
4.4.1	RNA velocity	55
4.5	ATAC-seq analysis pipeline	55
4.6	tRNA-seq analysis pipeline	55
5	Bulk RNA-seq analysis of PRS inhibitors	56
5.1	Introduction	56
5.2	Results	58
5.2.1	Dose response curves	58
5.2.2	Synergy with existing MM treatment	58
5.2.3	Bulk RNA-seq	58
5.2.4	Experiment overview	58

5.2.5	Effect of carfilzomib on WT cells	58
5.2.6	WT AMO-1 cells	58
5.2.7	Carfilzomib resistant cells	58
5.2.8	Amino acid starvation response	58
6	Single-cell RNA-seq analysis of PRS inhibitors	59
6.1	Introduction	59
6.1.1	Experiment overviews	60
6.2	Data processing	61
6.2.1	Analysis overview	62
6.2.2	Annotation of re-integrated data	64
6.3	Results	69
6.3.1	Newly diagnosed MM	69
6.3.2	Relapsed MM	69
6.4	Myeloma bone marrow classifier	69
7	tRNA-seq analysis of PRS inhibitors	70
7.1	Introduction	70
7.1.1	Experiment overview	70
7.2	Data processing	70
7.2.1	Quality control and filtering	70
7.3	Results	70
7.3.1	tRNA results	70
7.3.2	mRNA results	70
7.3.3	Multi-omics factor analysis	70
7.4	PRS inhibition general discussion	70
8	Epigenetic reversal of drug resistance in MM	71
8.1	Introduction	71
8.1.1	Experiment overviews	71
8.2	Dose response curves	71
8.3	Bulk RNA-seq	71
8.4	Single-cell RNA-seq	71
8.5	Proteomics	71
8.5.1	CyTOF	71
8.5.2	Total proteomics (LC-MS/MS)	71
8.5.3	Phosphoproteomics	71
8.5.4	Ubiquitinomics	71
8.6	ATAC-seq	71
8.7	Multi-omics factor analysis	71
8.8	TRIM24i general discussion	71

Appendices**A Epigenetic compound screen** **73****References** **74**

List of Figures

1.1	Hematopoietic system cell differentiation	2
1.2	Structure of the proteasome	8
1.3	DNA stucture and packaging.	10
1.4	Bulk RNA-seq outline	12
1.5	Drop-seq schematic	13
2.1	Multi-tRNA synthetase structure	20
2.2	Prolyl-tRNA synthetase inhibitor chemical structures	27
2.3	Halofuginone and the amino acid response diagram	30
3.1	TRIM24i structure	35
4.1	scRNA-Seq pseudoalignment pipeline flowchart	49
4.2	Benchmark Salmon Alevin Knee Plot	51
4.3	Benchmark Kallisto Bus Rotated Knee Plot	52
4.4	F1, Precision and Recall Bar Charts	53
4.5	Distribution of F1 scores	53
4.6	Benchmark Clustering Analysis	54
5.1	Halofuginone and NCP26 structures	57
6.1	Erythrocyte removal from integrated scRNA-seq datasets	63
6.2	Automated annotation of scRNA-seq data	65
6.3	MM cluster manual annotation- newly diagnosed MM	67
6.4	MM cluster manual annotation- relapsed MM	68
6.5	scRNA-seq composition analysis- newly diagnosed MM	69

List of Tables

1.1	Timeline of treatment options for multiple myeloma	6
3.1	Resuspension buffer recipe	37
3.2	Lysis buffer recipe	38
4.1	Carol diagram- benchmark gene expression definitions	52
6.1	Total cells, the number of cells passing filter, and the number of cells passing filter once erythrocyte clusters were removed across all samples for each patient.	64
6.2	Manual annotation markers	66

List of Abbreviations

MM	Multiple Myeloma
BM	Bone marrow
MGUS	Monoclonal gammopathy of unknown significance
SMM	Smoldering multiple myeloma
PI	Proteasome inhibitor
IMiDs	Immunomodulatory imide drugs
ER	Endoplasmic reticulum
UPS	Ubiquitin proteasome system
UPR	Unfolded protein response
DNA	Deoxyribonucleic acid
RNA	Ribonucleic acid
tRNA	Transfer RNA
NGS	Next generation sequencing
WGS	Whole genome sequencing
RNA-Seq	Ribonucleic acid sequencing
scRNA-Seq	Single cell RNA-Seq
dscRNA-Seq	Droplet-based scRNA-Seq
CB	Cellular barcode
UMI	Unique molecular identifier
LC-MS/MS	Liquid chromatography with tandem mass spectrometry
PCA	Principle component analysis
DMSO	Dimethyl sulfoxide
UMAP	Uniform Manifold Approximation and Projection
tSNE	t-distributed Stochastic Neighbor Embedding
NK	Natural killer

aaRS	Aminoacyl tRNA synthetase
EPRS	Glutamyl-prolyl-tRNA synthetase
ProRS	Prolyl-tRNA synthetase
MSC	Multi-tRNA synthetase
AIMP	aaRS interacting multifunctional proteins
FF	Febrifugine
HF	Halofuginone

1

Introduction

1.1 Overview

...

1.2 The adaptive immune system

Humans are exposed to millions of potential pathogens every day and therefore require defences to be able to protect themselves against infection. These defences can be innate or adaptive. An example of an innate defence is the skin acting as a physical barrier between the outside world and the body. Another example of an innate defence is non-specific engulfing (phagocytosis) of foreign pathogens by macrophages (a type of white blood cell). Innate responses are relied upon as the first line of defence, however sometimes a more sophisticated, specialised response is required- called the adaptive immune response. (REF-mol biology of the cell).

Adaptive immune responses are specific to the pathogen that induced the response and are dependent on B cells and T cells, two major classes of lymphocytes (a class of white blood cell). Two classes of adaptive immune responses exist: antibody responses, co-ordinated by B cells, and cell mediated immune responses, co-ordinated by T cells. T-cell-mediated immune responses recognise foreign antigens (antibody generators; substances capable of eliciting an immune response by stimulating B or T cell activation) on the surface of cells and can either kill the pathogen-infected cells or stimulate B cells or phagocytes to help eliminate the pathogen.

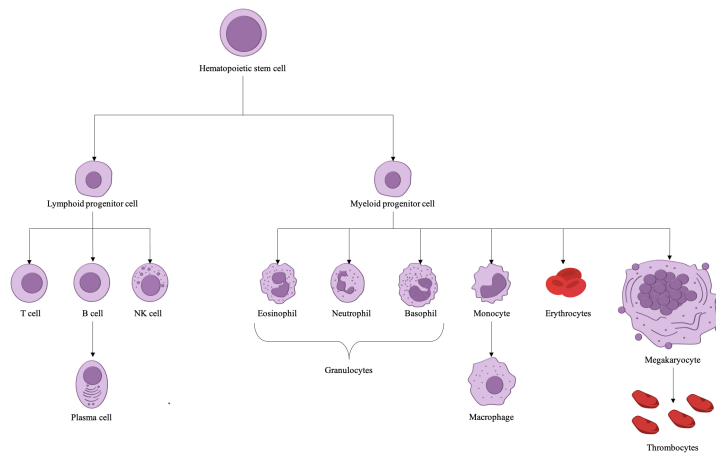


Figure 1.1: Hematopoietic stem cell (HSC) cell differentiation. HSCs divide into myeloid or lymphoid progenitor cells. Dendritic cells and a number of precursor states have been ommitted.

In antibody responses, B cells and plasma cells secrete antibodies, also known as immunoglobulins. Immunoglobulins are large Y-shaped proteins, which recognise and bind to the specific foreign antigen on the pathogen which stimulated their production. Binding of immunoglobulins to antigens renders the virus or microbial toxin inactive as it blocks their ability to bind to host cells. Additionally, antibody binding makes it easier for phagocytic cells to ingest the pathogen.

1.2.1 Plasma cells

Plasma cell development

Stem cells are precursor cells which can give rise to at least one type of differentiated (mature) cell, with the capability of indefinite self-renewal. Hematopoietic stem cells (HSC) are stem cells that give rise to all the cells of the hematopoietic system. Two predominant cell populations are produced by HSCs: the common myeloid progenitor (CMP) and the common lymphocyte progenitor (CLP). CMP differentiation produces erythrocytes (red blood cells), mast cells, monocytes, macrophages, neutrophils, eosinophils, basophils and myeloid dendritic cells. CLP differentiation results in B cells, T cells, natural killer (NK) cells and lymphoid dendritic cells.

Most B cells die in the bone marrow soon after developing, however some will develop in the bone marrow, where initial stages of maturation occur and then migrate to secondary lymphoid organs, such as the spleen. Within secondary lymphoid organs, numerous critical decisions on B cell fate are made, involving complex transcriptional networks, cell interactions, gene rearrangements, and mutations[1, 2]. Upon antigenic-stimulation, naive B cells differentiate into memory B cells or plasma cells. Terminally differentiated plasma cells are the final effectors of the B cell lineage, each dedicated to secreting large amounts of a single type of antibody. Plasma cells have an extensive rough endoplasmic reticulum (ER), and have numerous genes involved in immunoglobulin secretion upregulated, including *XBP-1* and *CHOP*[3], to enable the production of copious amounts of antibody. Plasma cells appear to consist of two distinct categories: short-lived plasma cells, which have life-spans of several months and are located in extrafollicular locales such as in medullary chords of lymph nodes or the red pulp of the spleen, and long-lived plasma cells, which have life-spans of decades and are mainly found in the bone marrow[4, 5].

1.3 Multiple myeloma

1.3.1 Multiple myeloma cells

Multiple myeloma is a malignancy of terminally differentiated plasma cells. It is characterised by aberrant proliferation of clonal, long-lived plasma cells in the bone marrow[6].

1.3.2 Epidemiology

Multiple myeloma accounts for 1-2% of all cancers and has the second highest incidence of hematological malignancies, after non-Hodgkin's lymphoma[7]. MM is rare in individuals under the age of 40, with the average age at time of diagnosis centering around 70[8, 9]. MM is more prevalent in males than females and is around twice as common in black populations than in Caucasian or Asian populations[10]. The average incidence rate is approximately 1-6 cases per 100000 individuals[8, 9,

11], with the highest age-standardised incidence rates in the regions of Australasia, North America, and Western Europe[12]. Five-year survival rate of MM patients is approximately 49%, whilst approximately a third of MM patients survive ten years or greater[13, 14].

1.3.3 Presentation

Precursor states

All cases of MM are preceded by asymptomatic precursor states, monoclonal gammopathy of unknown significance (MGUS) and smoldering multiple myeloma (SMM). However, only some patients with SMM or MGUS progress to active MM.

MGUS is a pre-malignant condition where patients have the presence of monoclonal immunoglobulins in their blood or urine, <10% clonal plasma cells in their bone marrow, but lack any myeloma-related end-organ damage[15]. Patients with SMM have between 10 and 60% clonal plasma cells in their bone marrow, serum monoclonal immunoglobulin of ≥ 3 g/dL, and like MGUS, have no signs of end-organ damage[16]. Progression risk of MGUS into symptomatic MM is about 1% per year, whilst progression risk of SMM to MM is higher, at around 10% per year for the first 5 years, after which it decreases[17, 18].

Active MM

There are multiple classifications of active MM. The International Myeloma Working Group's definition[19] is as follows: Greater than 10% clonal plasma cells located in the bone marrow and one or more myeloma-defining event or biomarker of malignancy. Myeloma defining events consist of evidence of end-organ damage that can be attributed to the surplus of M protein and clonal plasma cells, namely the CRAB features:

- Hypercalcemia
 - Serum calcium > 1 mg/dL higher than the upper limit of normal, or
 - Serum calcium > 11 mg/dL

- Renal insufficiency
 - Creatinine clearance < 40 mL per min, or
 - Serum creatine > 2 mg/dL
- Anemia
 - Hemoglobin value of > 20 g/L below the lower limit of normal, or
 - Hemoglobin value < 100 g/L
- Bone lesions
 - One or more osteolytic lesions on skeletal radiography, CT or PET-CT

Biomarkers of malignancy include greater than or equal to 60% clonal plasma cells in the bone marrow, an involved:uninvolved serum free light chain ratio greater than or equal to 100, and more than one focal lesion on an MRI study[19].

It is currently unclear what causes the malignant transformation between precursor states and active MM. However certain factors have been identified as risk factors, including point mutations, a large array of up-regulated transcription factors, and numerous immune events.

1.3.4 Treatment of multiple myeloma

Multiple myeloma may be an incurable disease, however it is treatable. In fact, in the last decade median survival time for newly diagnosed MM patients has almost doubled[20]. Novel therapeutic advances have contributed to this improvement (Table1.1).

1.3.5 Proteasome inhibitors

Proteasome inhibitors have contributed greatly to the improved prognosis of MM since their introduction into treatment regimes. The first-in-class proteasome inhibitor bortezomib (Velcade[®]) was approved by the FDA in 2003 as a single-agent for injection of relapsed MM[28]. Since then it has been approved for use

Year	Treatment	Usage	Ref
1958	Melphalan	The alkylating agent melphalan was first used in plasma cell myeloma in 1958.	[21]
1960s	Corticosteroids	Placebo-controlled double-blind trial of prednisone in multiple myeloma. Combinations of prednisone and melphalan showed an increased survival over melphalan alone. Dexamethasone and prednisone have become a cornerstone in the treatment of multiple myeloma.	[22, 23]
1980s	Stem-cell transplantations	Numerous successful allogenic and autologous bone marrow transplantations in patients with multiple myeloma	[24–27]
2003	Proteasome inhibitors	Bortezomib, a first-in-class proteasome inhibitor, was first approved by the FDA for use in relapsed and refractory multiple myeloma. In 2008 it was approved for patients with no prior treatment. Carfilzomib was approved in 2012 for advanced MM and later in 2015 for treatment of relapsed MM. The oral proteasome inhibitor, ixazomib, was approved as a combination treatment with lenalidomide and dexamethasone in 2016 for people who have received at least one previous treatment.	[28–30]
2006	IMiDs	The antitumour activity of thalidomide was demonstrated in 1999, this led to the development of lenalidomide, the first approved immunomodulatory imide drug (IMiD) for use in multiple myeloma. Currently, thalidomide, lenalidomide and pomalidomide are approved for use in multiple myeloma	[31–33]
2015	Monoclonal antibodies	In 2015, daratumumab, an anti-CD38 monoclonal antibody and elotuzumab, an anti-SLAMF7 monoclonal antibody, were approved for MM treatment.	[34, 35]

Table 1.1: Timeline of treatment options for multiple myeloma. Listed by first usage or FDA approval for MM.

in combination therapies. Bortezomib in combination with melphalan-prednisone proved to be superior to the previous standard of care for patients ineligible for HDT-ASCT of melphalan-prednisone alone, increasing time until tumour progression[36]. The combination of bortezomib, dexamethasone and thalidomide was also shown to

be superior to previous standard of care for patients prior to ASCT[37]. In 2010, bortezomib was approved as a frontline therapy for treatment-naive MM patients. Since then, two more proteasome inhibitors have been approved, carfilzomib and ixazomib. Carfilzomib is structurally and mechanistically different to bortezomib and shows activity on bortezomib resistant primary MM cells[37]; it is approved for relapsed or refractory MM.

The ubiquitin-proteasome system

Proteasome inhibitors work by blocking the action of the proteasome in the cell. Misfolded proteins can be harmful to a cell, so the combined activity of molecular chaperones, which aid in protein folding, and the ubiquitin-proteasome system (UPS), which acts to digest misfolded proteins, is needed to prevent massive protein aggregation. Unneeded, misfolded or damaged proteins are tagged with lysine-48-linked poly-ubiquitin chains, marking them for degradation by the proteasome (Figure 1.2a). The proteasome is sometimes described as a complex ‘protein destruction machine’. The proteasome consists of the 20S core particle, a central hollow cylinder, and the 19S regulatory caps associated with each end of the cylinder. The 19S regulatory caps perform substrate recognition, deubiquitination, unfolding and threading of the protein substrate into the 20S core. The core is made up of four stacked heptameric ring structures. The outer rings are responsible for docking to the 19S cap and for acting as a gate to the inner rings. The inner rings consist of seven β subunits, containing inward-facing protease active sites for degrading proteins[38, 39] (Figures 1.2a and 1.2b).

1.4 Drug resistance in multiple myeloma

... Lit review??

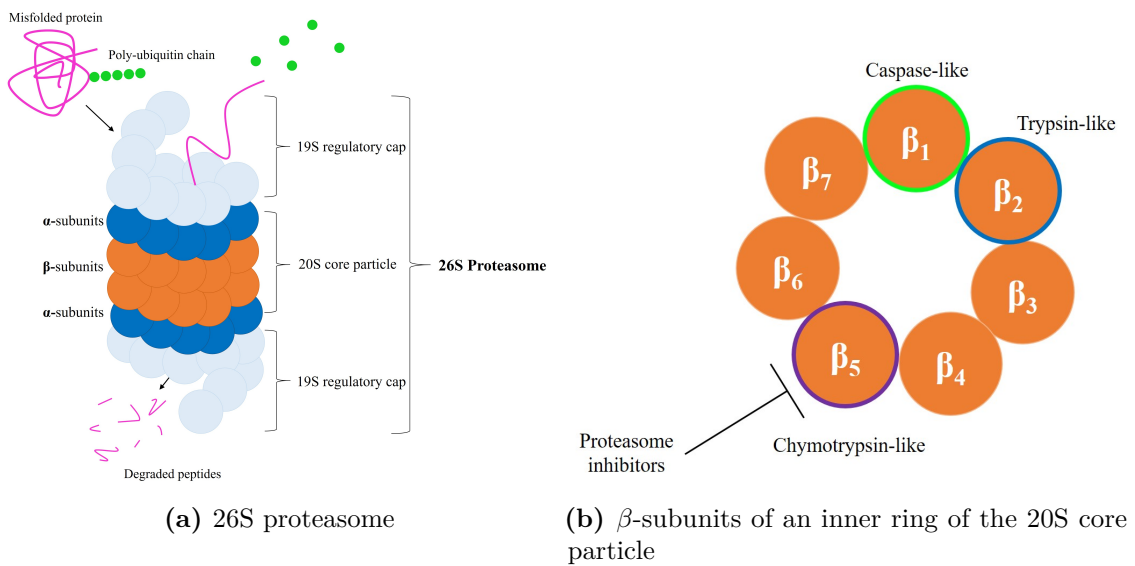


Figure 1.2: Structure of the proteasome. 1.2a shows the structure of the 26S proteasome, comprised of the 19S regulatory caps and 20S core particle. A misfolded protein tagged with a poly-ubiquitin chain is recognised by the 19S regulatory cap, which cleaves the ubiquitins from the protein and threads the protein through to the core, where it is degraded into small peptides. The 20S core particle is made up of two outer rings of α -subunits and two inner rings of β -subunits. 1.2b shows the β -subunit arrangement in one of the inner rings of the 20S particle. β_1 (caspase-like), β_2 (trypsin-like) and β_5 (chymotrypsin-like) are the proteolytically active subunits. Proteasome inhibitors are designed to primarily inhibit β_5 .

1.5 Transcriptomics, proteomics and epigenomics

It has been shown that changes in the genome, transcriptome, epigenome and proteome all contribute to acquired-drug resistance in myeloma. Therefore, to sufficiently investigate the multiple layers driving this development of resistance, a multi-omics approach must be employed.

1.5.1 DNA and the genome

The genome is the genetic material of an organism, it consists of deoxyribonucleic acid (DNA). DNA consists of two polynucleotide chains (or strands), running anti-parallel to each other, held together in a double helix structure by hydrogen bonds. Nucleotides are composed of a five-carbon sugar (deoxyribose for DNA), attached to one or more phosphate group (a single phosphate group in the case of DNA) and a nitrogenous base. Nucleotides are covalently linked to form an alternating sugar-phosphate backbone, with bases extending from each sugar towards the inside of the double helix. Nucleotides contain four different types of bases: adenine (A), cytosine (C), guanine (G) and thymine (T). The two DNA chains are held together by hydrogen bonds via complementary base pairing between the bases of the strands, A pairing with T and G pairing with C. Often sections of DNA are denoted as their sequence of A, C, T and Gs (in order reading from the 5' to 3' direction).

Every individual has approximately 6 billion base pairs of DNA per cell, which would amount to about 2 metres of DNA if laid end-to-end. The nucleus of a human cell is approximately 6 μm in diameter, therefore chromosomal DNA must be folded tightly to fit. DNA packaging is a complex task involving numerous specialised proteins. Negatively charged DNA is complexed with an octomer of positively charged proteins called histones to form nucleosomes. The histone core is made up of eight subunits, two copies of H2A, H2B, H3 and H4 subunits. DNA wraps tightly around the histone core 1.65 times. Linker DNA connects adjacent nucleosomes, to resemble ‘beads on a string’. Nucleosomes fold tightly to form 30nm chromatin fibre, which in turns forms loops averaging 300nm in length. This fibre is folded and compressed again to form fiber 250nm in width with loops of 700nm

in length. Tight coiling of this fiber forms the single chromatids of chromosomes [40, 41]. Human cells contain 23 pairs of chromosomes.

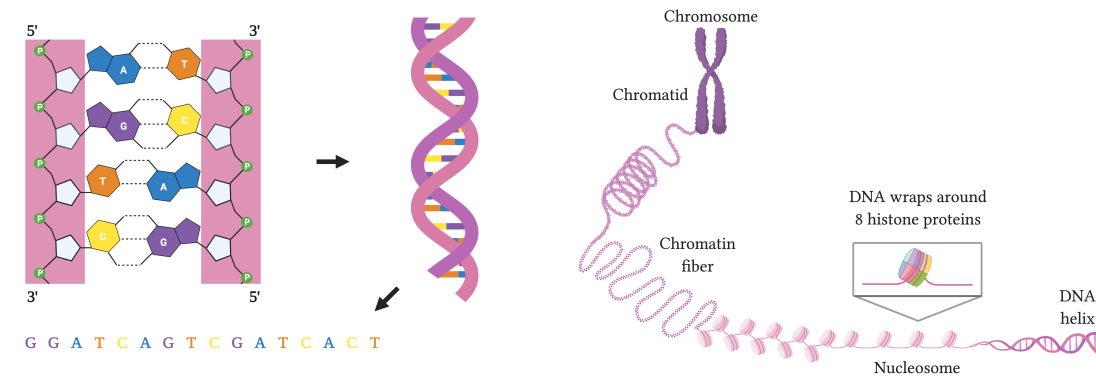


Figure 1.3: 1.3a shows the DNA nucleotides and the DNA double helix structure. DNA consists of two polynucleotide chains. Nucleotides are covalently linked to one another, forming a sugar-phosphate backbone. They contain one of four bases adenine (A), cytosine (C), guanine (G) and thymine (T). DNA strands are held together by hydrogen bonds between complementary base pairs, A pairing with T and G pairing with C. Sections of DNA are often read by their sequence of bases from the 5' direction to the 3' direction. 1.3b shows how chromosomal DNA is packaged in the cell. DNA wraps 1.65 times around an octomer of histone proteins, to form a structure called a nucleosome. Nucleosomes are linked by linker DNA to form a structure that resembles ‘beads on a string’. Nucleosomes fold to create chromatin fiber. This in turn forms loops and coils tighter and tighter until it makes up the single chromatids of chromosomes.

Created with BioRender.com.

The complete genome is made up of coding DNA (genes), non-coding DNA, as well as mitochondrial DNA and ribosomal DNA. An alteration in the nucleotide sequence of the genome is called a mutation. There are a number of types of mutations, including insertions, deletions, inversions, substitutions and duplications. A technique called whole genome sequencing (WGS) can be used to determine the sequence of nucleotides in an individual’s DNA and therefore it can be used to determine any variations in the genome.

1.5.2 The epigenome

Epigenetics is the study of any heritable phenotypic changes that do not involve alterations of the DNA sequence itself. Epigenetic changes include histone modifications, DNA methylation and chromatin remodelling. These changes occur at the

chromatin level and include DNA methylation, histone modification, and chromatin remodelling. These epigenetic changes are described in more detail below:

1.5.3 The transcriptome

Transcription is the first of many steps in gene expression. During transcription, the enzyme RNA polymerase reads a DNA sequence and produces an anti-parallel, complementary ribonucleic acid (RNA) strand. The transcriptome is the set of all RNA transcripts of an individual. RNA is a nucleic acid similar to DNA. Like DNA it has a sugar-phosphate backbone and 4 different types of bases attached to each sugar. However unlike DNA, RNA is single-stranded, it contains the sugar ribose instead of deoxyribose, and the nucleotide uracil (U) instead of thymine (T). There are many types of RNA, such as messenger RNA (mRNA), transfer RNA (tRNA), and ribosomal RNA (rRNA). RNA-seq is frequently used to study the transcriptome (outlined in section 1.5.5).

1.5.4 The proteome

Translation...

CyTOF and LC-MS/MS are often used to examine the proteome (section 1.5.8 and section 1.5.9).

1.5.5 RNA-seq

Modern RNA sequencing (RNA-seq) implements next generation sequencing (NGS) technology to analyse RNA across the transcriptome of a biological sample and allows for the quantification of gene expression.

Bulk RNA-seq

Bulk RNA-seq measures the average expression across a sample. Creating a bulk RNA-seq library involves isolating RNA from a biological sample, filtering for a specific type of RNA (most commonly mRNA), fragmentation of RNA into fragments, reverse transcription of the fragments to generate a complementary

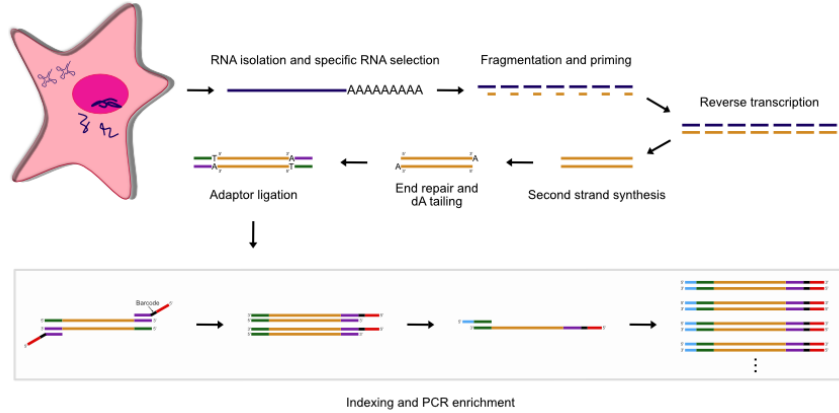


Figure 1.4: Outline of bulk RNA-seq library prep. Cells are lysed and RNA is extracted. The specific RNA of interest is selected and enriched, for example selecting for mRNA using polyA selection or ribo-depletion. The mRNA is fragmented into smaller pieces of RNA. First and second stranded cDNA are reverse transcribed from the RNA fragments using random primers. The ends of the cDNA are repaired and dAMP (dA) tails are added to the 3' end of the DNA. Adaptors are ligated to the 3' and 5' end of the cDNA. These adaptors contain complementary sequences that allow the fragments to hybridize to the flow cell during sequencing. Universal (P5/i5) and index (P7/i7) primers are added to the adaptor ligated DNA. The libraries are then amplified using PCR and cleaned-up, ready for sequencing.

DNA (cDNA) library, end repair and adaptor ligation of the cDNA library, followed by PCR amplification ready for sequencing.

Single-cell RNA-seq

Single-cell RNA-seq (scRNA-seq) measures gene expression for each individual cell across a population of cells and therefore provides information on clonal diversity that may be lost when pooling cells into bulk samples. Since its inception in 2009[42], there have been numerous scRNA-seq techniques, such as SMART-seq2[43], Drop-seq[44], STRT[45] and inDrops[46]. scRNA-seq library preparation shares many steps with bulk RNA-seq workflow, however preliminary steps are required to isolate single cells and track them (??/ barcode) individually.

For droplet-based scRNA-seq (dscRNA-seq) methods, single cells are isolated using microfluidic devices by individually encapsulating them in aqueous droplets contained in oil. Below, a dscRNA-seq method, Drop-seq, is outlined (Figure 1.5).

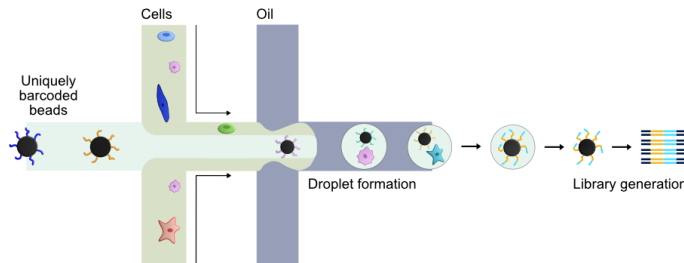


Figure 1.5: Outline of Drop-seq, a droplet-based scRNA-seq method. A microfluidic device combines two aqueous flows, one containing cells and the other containing barcoded primer beads suspended in lysis buffer. The two aqueous channels flow across an oil channel to form aqueous droplets surrounded by oil. Relatively few droplets contain both a cell and a bead. Following droplet formation, the cell is lysed and its mRNAs are released, which then hybridise to the primers on the bead surface. A reagent is added to break up the droplets and the beads are collected and washed. The mRNAs are reverse-transcribed into cDNAs, generating a set of “STAMPS” (single-cell transcriptomes attached to microparticles) and template switching is used to introduce a PCR handle. The barcoded STAMPS can then be amplified using PCR.

1.5.6 ATAC-seq

...

1.5.7 Next generation sequencing

Next generation sequencing (NGS), differs from its predecessors in that it is highly scalable and massively parallel. With NGS you can rapidly sequence the entire genome if desired. It is quicker and cheaper than traditional Sanger sequencing, and progressed data output from the kilobase range up to potentially multiple terabases per run.

1.5.8 CyTOF

...

1.5.9 Liquid chromatography with tandem mass spectrometry

Liquid chromatography with tandem mass spectrometry (LC-MS/MS) based proteomics is a popular analytical technique to measure the protein abundance of

a sample. The general steps for LC-MS/MS-based proteomics include: cell lysis, protein extraction, protein digestion using an enzyme to cleave proteins into peptides, peptide purification, and analysis by mass spectrometry. The resultant data includes mass and charge (m/z) information and peak intensities. Software is then employed which performs database searches and calculates the most likely peptide for each peak. From this data, protein abundance can then be calculated and normalised.

LC-MS/MS-based proteomics can also be used to search for specific proteins within the proteome. For example, immobilized metal affinity chromatography (IMAC) can be used to enrich for phosphorylated peptides (phosphoproteomics), and anti-ubiquitin antibodies can be used to enrich for ubiquitinated peptides (ubiquitinomics).

1.6 Summary

1.7 Aims

This thesis aims to characterise the changes driving proteasome-inhibitor resistance in multiple myeloma and identify possible mechanisms of reversing resistance. Chapter 2 gives background to the project, it reviews the literature surrounding drug resistance in MM and outlines preliminary work performed in the lab, that birthed this project. Chapter 3 outlines the methodology used in this work. Chapter 4 outlines the computational workflows generated to support this work and gives the results of a benchmark conducted to analyse the effectiveness of a computational pipeline developed. Chapter ?? describes how a lead epigenetic compounds was selected, analysing results from bulk RNA-seq data and validating previous compound screen results with dose response curves. Chapter ?? delves deeper into the drivers of changes in drug resistance and the mechanism of action of TRIM24i on resistant cells by looking at an array of multi-omics data.

2

Aminoacyl tRNA synthetases and Halofuginone

2.1 Introduction

Aminoacyl tRNA synthetases (aaRS) are a highly-conserved family of enzymes, responsible for “charging” tRNAs with their cognate amino acid. Human cytoplasmic aaRSs are either “free” as individual species or bound in a macromolecular complex, comprised of eight aaRSs and three auxiliary proteins, known as the multi-tRNA synthetase complex (MSC). On top of their canonical enzymatic role, aaRSs also engage in non-enzymatic functions in numerous pathways, including angiogenesis, inflammation and metabolism. Often species are released from the MSC to regulate these non-canonical activities. aaRSs have been shown to be involved in numerous diseases, including cancer. Initially, due to their high fidelity and complex evolution over millennia, aaRSs were seen as an attractive drug target for antimicrobials, to enable specifically targeting microbial aaRSs with minimal effects on human cells. The mechanism of action of Febrifugine (FF), a quinazoline alkaloid that has long been used as an antimalarial remedy, has recently been revealed; it acts as a competitive inhibitor of ProRS (part of the bifunctional glutamyl-prolyl-tRNA synthetase enzyme; EPRS), responsible for charging tRNA^{Pro} with proline. Although it has potent antimalarial effects, Febrifugine exhibits high liver and gastrointestinal (GI) toxicity, so cannot be used as a widespread drug, therefore several analogues of Febrifugine were developed in the hope of minimizing toxicity to the host’s cells.

One such analogue, Halofuginone (HF) was synthesized and was shown to have the most potent antimalarial properties of all the derivatives, with lower toxicity to the host than Febrifugine, but still some liver toxicity and GI side effects remain. Halofuginone has been applied to and showed promise in many other non-parasitic diseases too. It has received orphan drug status for scleroderma and HIV-Related Kaposi's Sarcoma. Recently, Halofuginone's application in various cancers has become of great interest, including but not limited to: metastatic brain tumours, bladder carcinomas, prostate cancer, renal carcinomas, hepatocellular carcinomas, lung cancer, breast cancer and multiple myeloma.

This review will introduce the structure and function of aminoacyl tRNA synthetases, provide an insight into their role in pathology and potential as therapeutic targets. EPRS1 and its inhibitors will be the primary focus, and exploring...

2.2 Function and structure of aminoacyl tRNA synthetases

Aminoacyl tRNA synthetases (aaRS) are an ancient family of ubiquitous enzymes, conserved across three major domains of life (but not present in viruses). They can be traced back prior to the “Last Universal Common Ancestor” (LUCA) [47]. aaRSs are essential for protein biosynthesis, and catalyse the first step in translation (see section 1.5.4). aaRSs catalyse the charging of tRNAs with their cognate amino acid. This is a two-step process. Firstly, aaRSs catalyse the formation of an aminoacyl-adenylate (activated amino acid) from their corresponding amino acid and an ATP molecule, releasing an inorganic pyrophosphate. Next, aaRSs catalyse the reaction between the aminoacyl-adenylate and their cognate tRNA to release an AMP molecule and generate an aminoacyl (charged)-tRNA, ready to be used by the ribosome to decode mRNA (see equation 2.1). An example of this process would be prolyl-tRNA synthetase (abbreviated to ProRS) charging tRNA^{pro} with proline.



Eukaryotes have 20 cytoplasmic aaRS and 20 nuclear-encoded mitochondrial aaRS. These are localised in distinct cellular compartments. aaRSs are often denoted by their one letter amino acid symbol, followed by ARS and either 1 (indicating they are cytoplasmic) or 2 (indicating they are mitochondrial), for example PARS1 for cytoplasmic ProRS. This review will focus on cytoplasmic aaRS enzymes. aaRS can be divided into two distinct classes based on the structure of the fold of their catalytic domains. Class I aaRS enzymes are functional monomers that contain a dinucleotide or Rossman fold (RF) of alternating alpha-helices and parallel beta-sheets. This fold is where ATP and amino-acid binding takes place and therefore facilitates the aminoacylation reaction. The active site of class I aaRS is marked by the signature motifs “HIGH” (His-Ile-Gly-His) and “KMSKS” (Lys-Met-Ser-Lys-Ser). Within the first half of the RF the HIGH motif helps to correctly position the adenine base of ATP and interacts with the phosphates. The second K of the KMSKS motif is thought to be involved in stabilising the transition state for the primary step of aminoacylation [48]. Amino acid recognition and binding takes place in the catalytic site when the KMSKS motif is open. The KMSKS loop closes after the aaRS binds ATP and the aminoacyl-adenylate is formed [49].

Class II aaRS enzymes are functional dimers or tetramers with an uncommon catalytic core, comprising seven anti-parallel beta-sheets, flanked by alpha-helices. Class II aaRS enzymes are defined by three conserved sequence motifs. Motif 1 is located at the interface of the dimer and enables oligomerization. Motifs 2 and 3 comprise part of the aminoacylation active site and facilitate amino acid/ ATP binding and adenylate formation. Motif 3 binds ATP, and motif 2 is involved in coupling ATP and the amino acid and then transferring the amino acid to the 3'-tRNA [49]. The distinct active-site structures of class I and II enzymes confer markedly different binding mechanisms for the aminoacylation reaction. For example, class I aaRSs bind the tRNA acceptor stem via the minor groove side and bind ATP in an extended conformation, whilst class II aaRSs bind the tRNA acceptor stem from the major groove side and bind ATP in a bent conformation. The two classes of aaRSs split the twenty amino acids into two groups. Val, Leu, Ile, Met,

Glu, Gln, Trp, Tyr, Arg and Cys are activated by their cognate class I aaRS; and Gly, Pro, Ala, Thr, Ser, Hist, Asp, Asm, Lys and Phe are activated by their cognate class II aaRS. Class I and class II can be further divided into different sub-groups, however that is beyond the scope of this review. The structural diversity of aaRSs is likely attributable to the need to exclude similar non-cognate amino acids and to discriminate the correct tRNA isoacceptor.

Both class I and class II aaRSs are multi-domain proteins- in addition to their catalytic domains, they include other domains such as their anti-codon recognition domain or an editing domain. The editing domain found in some aaRSs is to ensure that the essential step of aminoacylation in protein biosynthesis is as accurate as possible, so incorrect amino acids can be removed from aminoacyl-adenylates or mischarged tRNAs [49]. Theoretically, it was estimated that mistranslation rate should be approximately 1 in 200 for amino acids differing by just a methyl group (such as valine and isoleucine) [50], however in-vivo work demonstrated that the error frequency is closer to 3 in 10,000 (approximately 1 in 3000) [51]. This suggested the existence of proof-reading capabilities of aaRSs, to account for the difference between observed and predicted error rates. Editing capability has since been shown to be of high functional importance to some aaRSs. For example, a study in mice in which there was a missense in the editing domain of AlaRS. The impaired proof reading activity of the enzyme lead to an accumulation of misfolded proteins, resulting in the activation of the unfolded protein response and substantial neurodegeneration [52]. Not all aaRSs possess editing activity, only about half do, however the high specificity of the active site of those aaRSs is enough to alleviate proofreading need.

2.2.1 Multi-tRNA synthetase complexes

Higher eukaryotes contain macromolecular complexes, which consist of nine enzymes and three auxiliary proteins, known as multi-tRNA synthetase complexes (MSC). The 11 cytoplasmic aaRSs not located in the MSC remain free as individual species. The nine cytoplasmic aaRS enzymes of the MSC are GluRS (EARS1), ProRS (PARS1), IsoRS (IARS1), MetRS (MARS1), GlnRS (QARS1), LysRS

(KARS1), ArgRS (RARS1), AspRS (DARS1), LeuRS (LARS1). GluRS and ProRS are covalently fused via triple repeats of WHEP domains to form a bifunctional enzyme, EPRS1. The non-enzyme component of the MSC consists of three aminoacyl-tRNA synthetase-interacting multifunctional proteins (AIMP), AIMP1, AIMP2 and AIMP3. Human MSCs contain more class II aaRS enzymes than other species, namely DARS1, KARS1, and PARS1, they also contain more auxiliary proteins. Human MSC components have several additional domains or motifs (Figure 2.1A), for instance GST-homology domains in EPRS, MetRS, AIMP1 and 2, and WHEP domains in EPRS and MetRS [53–55].

The structure of human MSC has not been fully elucidated, however some sub MSC-complex structures have been revealed. LysRS forms a homodimer and is anchored to the N-terminal peptide region of AIMP2 within the main body of the MSC. MetRS, AIMP3, EPRS1 and AIMP2 are compactly linked through their GST-homology domains. ArgRS, GlnRS and AIMP1 assemble into a heterotrimeric complex [53–55]. A proposed bisymmetrical model of the human MSC, via homodimerization of AspRS and ProRS, is shown in Figure 2.1B, based on subcomplex and interaction data [56–58]. This hypothesis proposes that the MSC is a super-complex of two identical, symmetrically arranged subunits (symmetrical along the y-axis in Figure 2.1B), each containing one copy of the constituent elements, except for LysRS which is present as a dimer in each subunit.

The function of the MSC was originally thought to be to increase efficiency of protein biosynthesis by localising aaRSs. Another proposed function of the MSC was to increase stability of its components. It has been shown using systematic depletion analysis that some of the components are in fact intrinsically less stable in isolation and dependent on their neighbours for stability [59]. More recently, examples have emerged where the MSC seems to work as a ‘molecular reservoir’ which can control the release of its components. The release of components from the MSC has been linked to numerous non-canonical pathways, including cell signalling, metabolism, inflammation and angiogenesis.

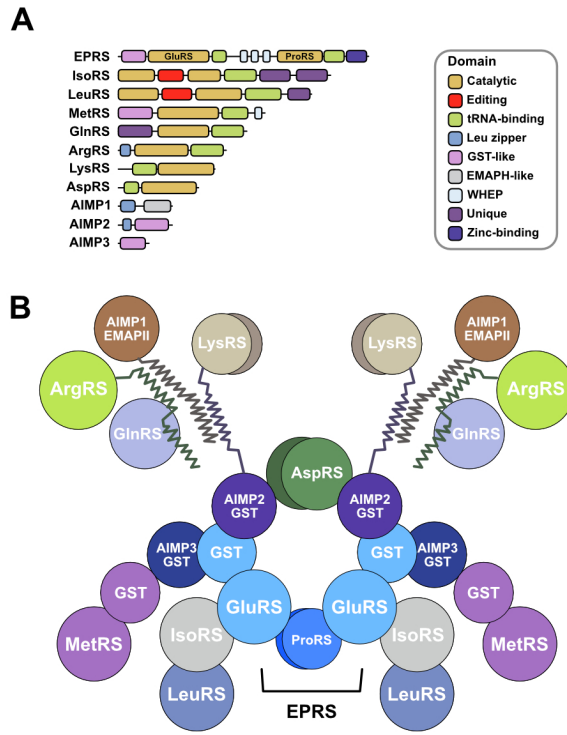


Figure 2.1: The human multi-tRNA synthetase (MSC) and its components. **A)** The domains of the aminoacyl tRNA synthetases and auxiliary proteins (AIMP1, 2 and 3) making up the human multi-tRNA synthetase (MSC). The bifunctional enzyme EPRS1 is made up of the class 1 enzyme GluRS and class II enzyme ProRS (dimer) covalently linked by three WHEP domains. **B)** Cartoon representation of a proposed bisymmetrical model structure of the human multi-tRNA synthetase complex (MSC). An adaption of a figure created by Myung Hee Kim and Sunghoon Kim [55].

Higher eukaryotes usually have extra-domains at the N- or C- terminus of aaRS enzymes compared with lower eukaryotes and prokaryotes, which may partly contribute to MSC assembly. Most human cytoplasmic aaRS enzymes have at least one new sequence extension or domain, most of which are dispensable for enzymatic activity, suggesting they may contribute to the non-canonical roles of aaRS. Additionally, aaRSs are often found in the nucleus of cells, where protein biosynthesis does not occur. The additional evolutionary complexity in human aaRSs and MSC seems to explain the increased physiological complexity and their functionality in non-enzymatic processes.

Examples of non-canonical MSC functionality include— LARS1 translocating from the MSC to lysosomes, facilitating mTORC1 activation [60]; KARS1 translo-

cating to the nucleus upon immune activation and activating MITF-dependent gene expression in mast cells [61]. Another example is EPRS1 release from the MSC in myeloid cells upon IFN- γ stimulation [62]. IFN- γ induces a network of kinase events (Cdk5, mTORC1 and S6K1 activation) which causes a two-step phosphorylation of two serines in the linker region of human EPRS, and causes its release from the MSC. EPRS1 combines with other proteins (namely NSAP1, L13a and GAPDH) to form the cytosolic IFN- γ activated inhibitor of translation (GAIT) complex, which represses translation of numerous inflammatory-related transcripts, including VEGFA and ceruloplasmin [63].

In addition to the enzymatic components of the MSC, the auxiliary proteins AIMP1, 2 and 3 are also involved in fundamental biological processes. AIMPs exhibit non-canonical functions aside from their roles as scaffolds in the MSC. AIMPs have been linked to numerous biological processes, including involvement in immune regulation, nervous system functions, viral replication, genome stability, angiogenesis, and cancer. AIMP1 interacts with RARS1 and facilitates incoming tRNA substrates to its catalytic site to enhance its enzymatic activity [64]. In addition to improving amino-acyl synthetase activity, secreted AIMP1 has also been shown to be involved in angiogenesis, inflammation induction, wound closure, and maintaining glucose homeostasis [65]. TGF- β and the DNA damage response have both been shown to cause phosphorylation of AIMP2 and disassociation from the MSC. Released AIMP2 has shown to act as a pro-apoptotic mediator and tumorigenesis suppressor via various pathways [66]. AIMP3 largely interacts with MARS1, and under conditions initiating the DNA damage response, MARS1 undergoes a conformational change that releases AIMP3 from the MSC [67]. Released AIMP3 acts as a tumour suppressor, translocating to the nucleus and upregulating expression of the tumour suppressor gene p53.

The functional and structural complexity of the MSC is still being revealed. The canonical and non-canonical functionality of MSC components promises an unexplored rich source of potential therapeutic targets, but also lends itself to associated pathology.

2.3 aaRSs in disease

With the diversity of functionality in human aaRSs comes an increase in functionality that can be associated pathologically with human disease. Structural and functional variations in aaRSSs' enzymatic and non-enzymatic activities have been linked to various human diseases. Changes in gene expression, copy number, mutations and genetic variations of aaRSs have been documented in relation to disease [49].

Charcot Marie Tooth (CMT) is a genetically and clinically-presenting heterogeneous group of hereditary peripheral neuropathies. CMT is characterised by progressive degeneration of distal sensory and motor neuron function [68]. Six aaRSs have been linked to CMT through dominant mono-allelic mutations, including GARS1 and YARS1, which are among numerous genetic-loci to have been linked causally to CMT. Drosophila models of CMT have demonstrated that CMT-causing YARS1 mutations lead to a conformational change in YARS1, leading to aberrant interactions with transcriptional regulators in the cell nucleus and aberrant expression of certain transcription factors [69].

aaRSs have also been implicated in autoimmune diseases. “Anti-synthetase syndrome” (ASS) is a heterogeneous group of autoimmune diseases, including interstitial lung disease (ILD), arthritis, idiopathic inflammatory myopathies, myositis and Reynaud’s phenomenon. Autoimmune antibodies against histidyl-, threonyl-, alanyl-, isoleucyl-, phenylalanyl-, glycyl-, tyrosyl-, asparaginyl-tRNA synthetase have been found in approximately 30% of all autoimmune patients. Dysregulation of aaRS has also been noted in other autoimmune diseases, for example multiple sclerosis and immune thrombocytopenia [70].

aaRSs have been linked to viral and bacterial infection. For example, it has been shown that viral infection leads to the phosphorylation of EPRS and dissociation from the MSC, ultimately blocking PCBP2-mediated mitochondrial antiviral signalling (MAVS) ubiquitination and inhibiting viral replication [71]. Additionally, HIV-1 infection leads to KRS release from the MSC, which is partially transported to the nucleus. Blocking this release reduced the infectivity of progeny virions, implying that HIV-1 utilizes a dynamic MSC for enhanced viral replication [72].

WARS1 was shown to be increased approximately 27-fold in sepsis patients with a bacterial infection compared with healthy controls. Following a range of infections by various pathogens, host monocytes were shown to rapidly secret WRS. The secreted WRS increased cell surface levels of CD40, CD80 and CD86, markers of macrophage activation [73].

2.3.1 aaRSs in cancer

A growing number of studies have implicated aaRSs and MSC components in tumorigenesis. Firstly, aaRS enzymatic activity is essential to sustain tumour growth. In cancer metabolism, biosynthesis of aminoacyl-tRNAs has been shown to be highly up-regulated [hu2013heterogeneity]. In cancer, we see often see dramatic rapid cell growth, this demands an intense increase in overall protein synthesis. To keep up with this demand, the canonical aminoacylation role of aaRSs is crucial as the first step in protein synthesis.

On top of the enzymatic role of aaRSs, their non-canonical functionality has also been associated with both promoting and inhibiting cancer. The hallmarks of cancer- enhanced growth signalling and proliferation, vascularization, metastasis, altered metabolism, and immune/tumour microenvironment invasion, all have links to tRNA synthetase function. Cancer cells require enhanced growth signalling and proliferation to maintain their rapid growth beyond the capacity of normal cells, several aaRSs have been linked to this aberrant growth signalling. GlyRS has been shown to be integral for cancer-promoting neddylation to occur, and reduced MetRS expression resulted in reduced tumorigenicity in p16INK4a-negative breast cancer cells *in vivo* [74–76]. For tumours to grow and metastasize they need to hijack existing vasculature to get blood flow to growing area, or make new vessels by promoting angiogenesis. Endothelial cells (EC) exposed to TNF- α or VEGF secrete ThrRS. ThrRS promotes EC migration and angiogenesis. Inhibition of ThrRS was shown to inhibit angiogenesis, with and without inducing the uncharged tRNA response [77, 78]. LysRS has been shown to support metastasis by increasing migration. Following phosphorylation by the MAPK pathway, LysRS binds to the 67kDa

membrane bound laminin receptor protein (67LR), preventing its degradation and sustaining laminin-dependent migration. Once bound to LysRS, 67LR also binds integrin $\alpha 6\beta 1$, which initiates ERK and paxillin signalling, increasing migration by altering cell-cell and cell-ECM adhesion.

aaRSs have also been linked to altering metabolism in cancer. To make rampant growth feasible, cancer cells adjust metabolism to meet energy demands and provide building blocks for biosynthesis. LeuRS activates the mTORC1 pathway, which controls translation and autophagy. Cancer cells utilize the mTORC1 pathway to proliferate more efficiently. The mTORC1 pathway also causes phosphorylation of EPRS and the release of it from the MSC. In adipocytes, released EPRS interacts with FATP1 and directs it to the plasma membrane. Inhibition of FATP1 leads to increased cell viability in breast cancer cell lines, and its expression correlates with decreased patient survival in triple negative breast cancer [79].

2.3.2 AIMP_s in cancer

As well as the association between aaRSs and cancer, AIMP_s have also been shown to play a role in signalling pathways relevant to numerous cancers. The MSC-bound aaRSs seem to predominantly promote tumorigenic functions when released from the MSC. In contrast, the AIMP_s bound with them seem to have more tumour-suppressive effects. AIMP2 has been shown to be a potent tumour suppressor, working via key regulators in the p53, c-Myc, Wnt, TGF- β and TNF- α signalling pathways. Loss of a single allele of AIMP2 in mice resulted in a far higher susceptibility to tumour formation [80]. AIMP1 has also demonstrated tumour-suppressive effects. In mouse xenograft models, administered AIMP1 was found to reduce tumour volume [81, 82]. AIMP1 has been shown to induce apoptosis of endothelial cells, such that it suppresses tumour vascularization [83]; it also stimulates anti-tumour immune responses, for example activating natural killer (NK) cells via macrophages, dramatically reducing lung metastasis of melanoma cells [84]. AIMP3 activates the tumour-suppressor gene p53 following DNA damage

or oncogenic stress. Loss of an AIMP3 allele results in higher susceptibility to spontaneous tumour formation [85].

2.4 aaRSs as therapeutic targets

aaRSs are considered very attractive drug-targets. Initially the interest in aaRSs as therapeutic targets arose with the detection of differences between prokaryotic and eukaryotic aaRSs. Thus, enabling specific targeting of microbial aaRSs with minimal effect on the homologous human aaRSs, making aaRS inhibitors attractive anti-microbial candidates. In the 1990s, Mupirocin (brand name Bactroban) was approved as an antibiotic for the topical treatment of bacterial skin infections. Mupirocin selectively inhibits bacterial IleRS, by simultaneously occupying the isoleucine and AMP binding sites and inhibiting aminoacylation [86]. Mupirocin has shown high selectivity for bacterial IleRS over mammalian IleRS (greater than 8000 fold) [87]. This conferred selectivity seems to be due to only a two-amino acid residue difference in the active site of eukaryotic and prokaryotic IleRS [88]. Another example is Kerydin (Tavaborole or AN2690), an anti-fungal used to treat onychomycosis, which targets fungal LeuRS. Kerydin is a boron-containing compound (Benzoxaborole) and the first drug to target an aaRS editing site. The boron atom of Kerydin binds to the terminal tRNA_{Leu} ribose, trapping tRNA_{Leu} in the editing site and causing a non-productive enzyme conformation, which inhibits protein biosynthesis. [[REF]]

2.4.1 Parasites

On top of the success of the druggability of aaRS enzymes for bacterial and fungal infections, aaRSs have also showed promise as an anti-parasitic target. Much like cancer, parasites are extremely reliant on protein synthesis to keep up with rapid cell growth and continuous proliferation, so are likely to be more sensitive to disruptions to aminoacylation. Additionally, the evolutionary distance between parasitic aaRSs and human aaRSs is quite large, in fact several parasites have bacterial-like protein translation pathways, not shared by humans [89]. Numerous aaRSs have previously shown promise as targets for anti-parasitic agents. Several naturally occurring

compounds target the AsnRS site of parasites, such as *Brugia malayia*, a nematode which causes Lympathic Filariasis. *Trypanosoma brucei* has also been shown to be susceptible to aaRS inhibition, for example by Benzoxaboroles targeting LeuRS, or by Aminoquinoles and Benzimidazoles targeting MetRs. The parasite *Plasmodium falciparum* has been shown to be affected by numerous aaRS inhibitors, including Mupirocin, Cladosporin and Febrifugine derivatives.

2.4.2 Febrifugine and its derivatives

Dichroa febrifuga has been used for centuries in Chinese medicine as an antimalarial remedy, it is considered one of the 50 fundamental herbs. In 1948, two quinazoline alkaloids, named Febrifugine (FF) and Isofebrifugine, were first isolated from the plant Dichroa febrifuga (Figure 2.2) [90], as part of a directive to find new anti-malarials from plant sources. Although Febrifugine has excellent anti-parasitic activity, it also has strong liver and gastrointestinal toxicity, limiting its use as a widespread therapeutic. This motivated the generation of Febrifugine derivatives with the hope of reducing off-target toxicity. The medical applications of the long-used traditional anti-parasitic agent Febrifugine and its derivatives have recently attracted much attention. Febrifugine derivatives have been used to treat malaria, fibrosis, inflammatory disease and cancer.

2.4.3 Halofuginone

One such analogue, a synthetic racemic halogenated derivative of Febrifugine, Halofuginone (HF; Figure 2.2), was synthesized in 1967 by American Cyanamid Company [zhang2017novel]. Halofuginone was found to have the most potent antimalarial activity of the FF analogues in vitro and affected all three stages of *P. falciparum* (ring stages, trophozoites and schizonts) with equal speed, unlike many other chemicals with antimalarial effects. The addition of bromine on the quinazoline ring in HF was found not affect the antimalarial properties of FF, whilst lowering the cytotoxicity for host cells compared to FF. However, HF does still demonstrate some toxicity to the liver, among other side effects, including

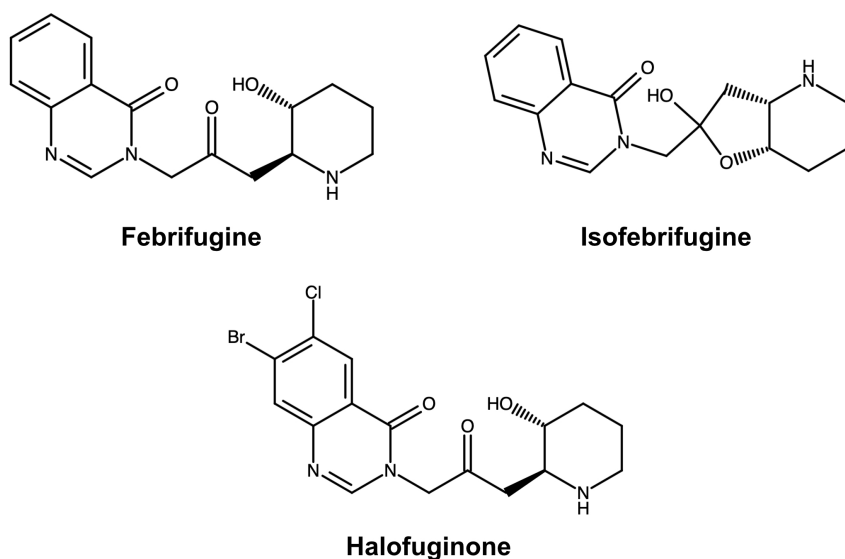


Figure 2.2: Chemical structures of prolyl-tRNA synthetase (ProRS/PARS1) inhibitors. Febrifugine and isofebrifugine were first isolated from *Dichroa febrifuga* in 1948. Halofuginone is a derivative of Febrifugine, first synthesized in 1967.

diarrhoea and vomiting [pines2015halofuginone]. In an attempt to reduce the side effects of HF and increase the therapeutic window, trans-enantiomers (2R,3S / +) and (2S,3R / -) of HF have been prepared. Although (-)-HF was found to have lower toxicity than its optical antipode, it was also found to be less efficacious than (+)-HF [91, 92]. This suggests that the biological activity and mammalian toxicity of HF reside with the same enantiomer, therefore there is no advantage to using a specific enantiomer over the racemic mixture.

Recently Halofuginone has been researched extensively in association with its applications to non-parasitic diseases. HF is FDA-approved as a feed additive for poultry to prevent coccidiosis from the protozoa *coccidian*. HF has also received orphan drug status for scleroderma and Duchenne muscular dystrophy. HF has undergone clinical trials as a potential therapeutic in a number of conditions, including cancer [93, 94].

Halofuginone's mechanism of action

Until the last decade, the mechanism of action of Halofuginone was unclear, until two papers from 2009 [95] and 2012 [96] elucidated HF's target and downstream

effects. Mouse TH17 cells were treated with HF or an inactive derivative, MAZ1310, for 3 or 6 hours and microarray analyses were performed. ATF4 target genes were found to be activated by HF expression, including Asns, Chop, eIF4Ebp, Gpt2, as well as amino acid transport genes, such as Slc6a9 and Slc7a3, both patterns that correspond with activation of the amino acid starvation response (AAR). Using western blots, the group also showed that GCN2 autophosphorylation was activated by HF treatment, further indicating HF activates the AAR pathway. This effect was not limited to TH17 cells, the AAR pathway was also activated by HF treatment in fibroblasts and epithelial cells [95]. However, this paper did not reveal how HF activated the AAR.

In 2012, the group demonstrated that HF and FF activate the AAR by competing with proline as potent inhibitors of tRNA^{pro} charging activity of EPRS1. Rabbit reticulocyte lysate (RRL) was used as an in-vitro translation system. Following supplementation with excess amino acids, only proline was shown to restore translation inhibited by HF in the RRL system. Moreover, HF-derivatives that were shown to be inactive in functional cell-based assays, such as MAZ1320, also lacked activity in the RRL assay. Together, this suggests that HF functionality is linked to blocking proline utilization. To further demonstrate that HF and FF affect proline utilization, the group synthesized DNAs encoding two epitope-tagged polypeptides, one encoding a proline-dipeptide (ProPep), the second encoding a proline-free peptide (NoProPep). HF and FF treatment prevented translation of ProPep, but had no effect on NoProPep translation [96].

Next the group investigated the effect of HF on prolyl-tRNA charging and the bifunctional enzyme EPRS1 (comprised of GluRS and ProRS fused together). The addition of EPRS from purified-rat-liver reduced the sensitivity of RRL to HF. They then investigated the inverse using siRNA-mediated knockdown to reduce EPRS levels in lung fibroblasts. Lung fibroblasts have high levels of EPRS endogenously, so are quite resistant to HF treatment. The reduction of EPRS levels sensitized the cells to HF treatment and AAR pathway activation—GCN2 autophosphorylation was induced as well as ATF4 response genes, such as CHOP and ASNS. Together

this established for the first time that EPRS is a critical target of inhibition for HF and FF, through which the compounds elicit AAR activation. The group demonstrated that HF inhibits EPRS in a competitive fashion with proline at the prolyl-tRNA synthetase active site. HF binding is an ATP-dependent process. ATP directly locks onto and positions HF onto human ProRS so that one part of HF mimics bound proline and the other mimics the 3' end of bound tRNA^{pro} [97]. Excess proline addition was shown to abrogate AAR activation and reversed the biological effects of HF [96].

By binding the active site of ProRS, HF blocks proline from binding and inhibits ProRS enzymatic activity. This results in an intracellular build-up of unaminoacylated (uncharged) tRNA^{pro}s, mimicking the cellular state of proline deficiency, thus triggering the amino acid starvation response. Uncharged tRNAs bind to the protein kinase GCN2 and stimulates its dimerization and autophosphorylation. Activated GCN2 phosphorylates eukaryotic translation initiation factor 2A (eIF2 α), this leads to a reduction in most protein synthesis, whilst increasing translation of ATF4. ATF4 is a transcription factor of the cAMP response element binding protein (CREB) and induces the expression of many genes involved in the integrated stress response (for example DDIT3/CHOP), amino acid synthetases and transporters, aminoacyl tRNA synthetases, and autophagy regulators (figure 2.3) [95, 98].

Halofuginone's downstream signalling pathways

— TO FILL in — To complete...

2.4.4 The application of Halofuginone in cancer

HF has exhibited anti-cancer effects in numerous studies and different cancers, including metastatic brain tumours, bladder carcinomas, prostate cancer, renal carcinomas, pheochromocytomas, hepatocellular carcinomas, esophageal squamous carcinomas, lung cancer and breast cancer [99–107]. HF has been shown to exert anti-cancer effects in numerous manners, including reducing tumour growth, reducing

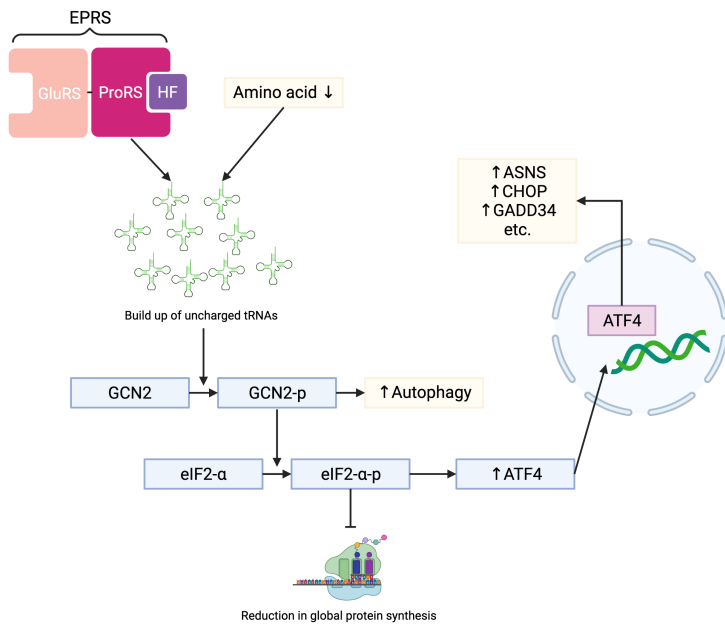


Figure 2.3: A diagram of Halofuginone's (HF) mechanism of action and relationship with the amino acid starvation response (AAR). HF binding with the catalytic site of prolyl-tRNA synthetase (ProRS) of the bifunctional aminoacyl-tRNA synthetase, EPRS, causes an accumulation of uncharged tRNAs, mimicking the same cellular environment as if the cell were amino acid deprived. Uncharged tRNAs bind to the cellular sensor GCN2 and cause it to autophosphorylate and activate. Activated GCN2 then phosphorylates eIF2- α . eIF2- α -p reduces global protein synthesis, except for mRNAs containing an upstream ORF cluster in their 5' untranslated region (UTR) which are efficiently translated upon eIF2-alpha phosphorylation [98], including the transcription factor ATF4. Upregulated ATF4 results in increased expression of many genes involved in stress responses (e.g. CHOP/DDIT3), amino acid metabolism, amino acid synthetases (e.g. ASNS) and aminoacyl tRNA synthetases. Figure created with Biorender.com

angiogenesis, activating autophagy and apoptosis, and disrupting the collagen network of tumours, among other mechanisms.

Halofuginone and multiple myeloma

As mentioned in section 1.3, multiple myeloma (MM) is an incurable cancer of plasma cells. Drug resistance is a massive problem in MM, with patients becoming resistant to drugs they've previously been treated with, cycling through treatment and relapse cycles. Therefore, identifying novel therapeutics for the treatment of MM is of critical importance.

Following the success of HF treatment in numerous preclinical cancer studies and the phase II study of HIV-related Kaposi's sarcoma [108], Leiba et al. (2012)

investigated the treatment of HF in multiple myeloma, both in-vitro and in-vivo [109]. 17 MM cell lines were treated for 48 hours with a range of HF concentrations. HF was shown to induce a reduction in cell viability in a dose-dependent manner across all 17 MM cell lines, with an IC₅₀ of approximately 100nM in most cell lines. The effect of HF on primary cells was then investigated. CD138+ cells from BM samples from five MM patients and PBMCs from two healthy donors were treated with a range of HF concentrations. A greater dose-dependent reduction in cell viability was seen in the primary MM cells compared to the healthy PBMCs, with an IC₅₀ ranging from 101-253nM for the MM cells. Demonstrating that, at this concentration range, HF specifically inhibits the viability of MM cells while having no significant effect on normal cells; this also gave a therapeutic window for HF in MM. Next, the group demonstrated that HF induces apoptosis in MM—HF treatment triggered caspase 3, 8 and 9 activities in MM cell lines in a dose dependent manner; it increased the quantity of apoptotic cells (Annexin V-FITC apoptosis assay); it caused an accumulation of cells in sub G1 phase of the cell cycle, associated with DNA fragmentation; and it elevated expression of the heat shock protein Hsp-90. They also showed that exogenous IL-6 and IGF-1, which are central for MM growth and survival, did not rescue HF-induced cytotoxic effects on MM cell lines, indicating that paracrine MM cell growth and the BM environment are unlikely to reverse the biological effects of HF.

The group also exhibited the anti-MM effects of HF in-vivo, using in a xenograft model of SCID mice injected with MM.1S cells. Once tumours reached sufficient size, mice were treated with either PBS or HF for five days a week for the duration of the experiment. HF treatment was found to inhibit tumour growth and increase overall survival compared to the control mice.

From this study, it is clear HF is effective against MM, and could show promise as a potential line of therapy in MM. The group used MM cell lines, mouse models and primary BM samples from MM patients. However, the primary BM samples were compared against healthy donor's PBMC cells and not MM patients own non-myeloma cells, so only limited conclusions can be drawn about HF's specificity

for MM cells over normal cells. Additionally, the cells were studied in isolation, the effect of HF on the MM immune microenvironment was not investigated. Also, the group did not show how HF was exerting its effect, whether, like in other studies HF, is activating the amino acid starvation response and inducing apoptosis, or working in some other way. AAR activation results in upregulated levels of the transcription factor ATF4. It would be interesting to explore the transcriptional landscape of MM cells and the tumour microenvironment following HF treatment, to see how AAR activation affects this.

2.5 Conclusion and future directions

Considering aaRSs are such a highly conserved and ancient family of enzymes, it is surprising how much about their structure and function is still unknown.

PROTACs...

3

Methods

3.1 Cell culture

3.1.1 AMO-1 cells

AMO-1 cells, plasma cells from a 64-year old female myeloma patient, were used as a model cell-line for multiple myeloma. Proteasome inhibitor-sensitive AMO-1 cells are referred to as WT cells. Bortezomib resistant (aBTZ) and carfilzomib resistant cells (aCFZ), believed to be AMO-1 cells were generated and gifted by the Driessen lab[110]. After typing these cells, they were found to be a mix of AMO-1 cells and L363 cells. AMO-1 cells were cultivated in RPMI-1640 medium (Thermofisher, UK), supplemented with 10% fetal bovine serum (FBS), 100 μ g ml⁻¹ streptomycin and 100 U/ml penicillin (P/S) and 2mM L-glutamine (Invitrogen, UK). Cells were passaged when they reached approximately 1.5-2 million cells per ml. AMO-1 cells are suspension cells and were split twice a week to approximately 0.5 million cells per ml.

3.1.2 L363 cells

After typing the cells gifted by the Driessen lab, they were found to be a mix of AMO-1 MM cells and L363 MM cells. In-house PI-resistant cell lines were by Dr James Dunford by continual and escalating drug exposure of drug-sensitive (WT) AMO-1 cells. However after these cells were typed, they were found to be L363 cells. This was due to the drug exposure selecting the L363 contaminant population over the AMO-1 cells, due to their natural increased resistance to PI, compared to

AMO-1 cells. Once this mistake made by our collaborators was noticed, WT L363 cells were purchased from (<INSERT HERE>). WT, aCFZ and aBTZ cells were cultivated in RPMI-1640 medium (Thermofisher, UK), supplemented with 10% fetal bovine serum (FBS), 100 μ g ml⁻¹ streptomycin and 100 U/ml penicillin (P/S) and 2mM L-glutamine (Invitrogen, UK), and kept in 100nM of their respective proteasome inhibitor. Cells were passaged when they reached approximately 1.5-2 million cells per ml. L363 cells are suspension cells and were split twice a week to approximately 0.5 million cells per ml.

3.2 Compounds

3.2.1 Proteasome inhibitors

<WHERE were they obtained> etc etc.

3.2.2 PRS inhibitors

Halofuginone (MAZ1392)

MAZ1805

NCP22

NCP26

ProSA

3.2.3 Epigenetic inhibitors

The Oppermann group has an epigenetic compound screening library, consisting of 144 compounds. The compounds were obtained XYZ <where did Jim get compounds> SGC???? A dual TRIM24/BRPF inhibitor was identified as a possible candidate to reverse drug-resistance in AMO-1 cells. The structure of the inhibitor is shown below in figure 3.1.

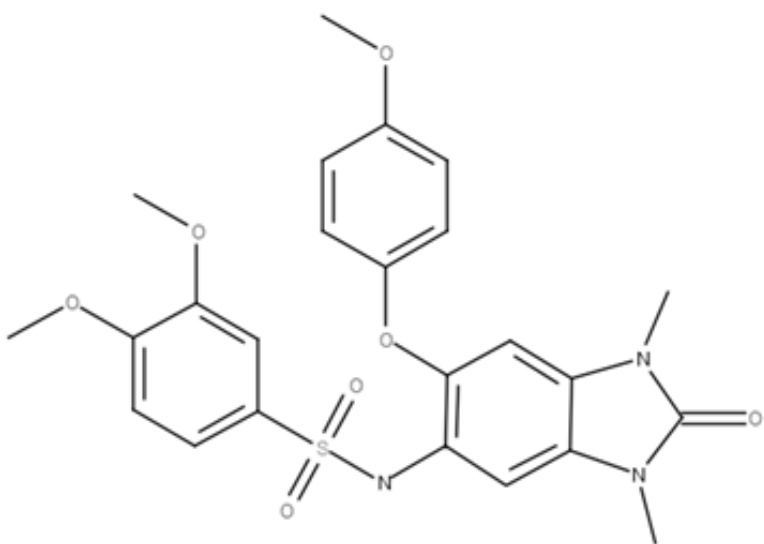


Figure 3.1: TRIM24 inhibitor chemical structure

3.3 Assays

3.3.1 Cell viability assays

10X presto blue (alamar??) was added in a 1:10 ratio to cells in suspension and incubated at 37°C for two to three hours. Plates were read [DETAILS OF MACHINE AND PROTOCOL, e.g. wavelength]

3.3.2 Dose response curves

90 μ l of cells in fresh media were seeded into 96-well plates a day prior to treatment with compound. A total of 10,000 cells were seeded into each well. No cells were placed in edge wells, to avoid edge effects. The following day, media 0% viability controls were placed in the first and last row. Drug concentrations were made up 1000x the desired final concentration in eppendorfs. Drugs were diluted 1 in 100 in 96 well round bottom plates with media and then 10 μ l was added to the 90 μ l of seeded cells in triplicate. Cells were treated with DMSO in triplicate as 100% viability controls.

3.4 Bulk RNA-seq

3.4.1 RNA extraction

RNA was extracted and purified using the Direct-Zol RNA MiniPrep kit (Zymo, USA), following the manufacturer's protocol. In brief, for each sample, approximately 100,000 cells were lysed in 300 μ l of TRIzol and the lysate was transferred to a microcentrifuge tube. 300 μ l of ethanol was added to the lysed samples and vortexed. The mixture was transferred to miniPrep columns and centrifuged at 10,000-16,000g for 30 seconds. The column was washed twice with 400 μ l of Direct-Zol pre-wash and once with 700 μ l of RNA wash buffer. The column was transferred to an RNase-free tube and eluted with 50 μ l of nuclease-free water and centrifuged.

The RNA concentration was quantified using a NanoDrop ND-1000 Spectrophotometer (Thermo Fisher Scientific, USA), and samples were stored at -80°C. Samples were normalised to 100ng with nuclease-free water.

3.4.2 RNA library preparation

NEBNext® Ultra II directional RNA library prep kit for Illumina® with TruSeq indexes was used to prepare RNA libraries, following the manufacturer's protocol. RNA concentration was normalised to 100ng with nuclease-free water, made up to 50 μ l. The NEBNext Poly(A) mRNA Magnetic Isolation Module (NEB, USA) was used to enrich poly-adenylated RNA. READ booklet in lab

The molarities of the libraries were determined by electrophoresis on a TapeStation (Agilent, USA).

3.5 Single-cell RNA-seq

3.5.1 Cell encapsulation

The Drop-Seq protocol[44] was followed for single-cell RNA-seq sample preparation. Cells were loaded into a microfluidics cartridge. Nadia, an automated microfluidics

device (Dolomite Bio, UK), performed cell capture, cell lysis and reverse transcription. Reverse transcription reactions were performed using ChemGene beads or (ATDBio beads 2020 onwards!!!! might need to change if reperform).

3.5.2 Library preparation

Beads were collected from the device and cDNA amplification was performed. The beads were treated with Exo-I prior to PCR. The amplified, purified cDNA then underwent fragmentation reactions. A TapeStation (Agilent, USA) was used to assess library quality. The samples were pooled together and split across multiple sequencing runs.

3.6 ATAC-seq

3.6.1 Cell lysis

Approximately 2 million cells were collected in 15ml falcon tubes for each condition. The cells were centrifuged at 300g for 5 minutes at 4°C and the supernatant was discarded. The cell pellets were resuspended in 1ml of cold PBS and centrifuged at 300g for 5 minutes at 4°C, the supernatant was then discarded. Fresh lysis buffer was prepared (see tables ??) with occasional gentle flicking. The falcons were then centrifuged at 500g for 10 minutes at 4°C. The supernatant (cytoplasm) was discarded, leaving the nuclei pellet.

Resuspension buffer	Volume (µl)
1M Tris-HCl (pH 7.5)	500
5M NaCl	100
1M MgCl ₂	150
Nuclease-free water	49,250
Total	50,000 (50ml)

Table 3.1: Resuspension buffer recipe

Lysis buffer	Volume (μl)
Resuspension buffer	940
10% non-iodet P40	50
10% tween 20	10
Total	1000 (1ml)

Table 3.2: Lysis buffer recipe

3.6.2 Transposition

Pellets were resuspended in 890μl transposition mix (500μl 2X TD buffer, 330μl 1X PBS, 10μl 10% Tween-20, 10μl 5% Digitonin, 40μl nuclease-free water). For each condition, 176μl was taken in triplicate and transferred to LoBind 1.5ml eppendorfs (Eppendorf, UK). 4μl Tn5 enzyme was added to each eppendorf. The samples were then incubated at 37°C for an hour at 500rpm.

3.6.3 DNA purification

Magic bead clean-ups were performed to purify the DNA. 220μl of magic beads was added to each tube (1.2X), vortexed, centrifuged for 1-2 seconds and incubated at room temperature for 5 minutes. Tubes were placed on a magnetic rack for 2 minutes, until the solution was clear. The liquid from the tubes was aspirated away, leaving about 10μl of liquid remaining. 200μl of 80% ethanol was dispensed over the beads, the tubes were vortexed, spun and placed back on the magnetic rack until the solution was clear and then the ethanol was aspirated away. This wash was repeated for a total of two ethanol washes. Following aspiration on the 2ndwash, an additional spin was performed and the tubes were placed back on the magnetic rack and any remaining liquid was aspirated away, to ensure all ethanol was removed. The beads were left to air dry for 3-5 minutes on the magnetic rack with the lids of the tubes open. The tubes were removed from the magnetic rack and eluted with 26μl 0.1X TE buffer (Zymo Research, UK). The tubes were vortexed, spun and left to incubate for 5 minutes at room temperature, before being placed back on the magnetic rack. The eluant was transferred to fresh LoBind tubes. The purified DNA was then stored at -20°C until PCR amplification was ready to be performed.

3.6.4 PCR amplification

20 μ l of purified DNA from each sample was mixed with 20 μ l nuclease-free water, 5 μ l ATAC-seq universal primer, 50 μ l Nebnext high fidelity 2X master mix and 5 μ l unique ATAC-seq index primer, and split across two PCR tubes. The PCR tubes were put in a thermocycler with a lid temperature of 103.5°C, they were heated to 72°C for 5 minutes, 98°C for 30 seconds, and then cycled at 98°C for 10 seconds, 63°C for 30 seconds and 72°C for 1 minute, 13 times. Samples were then held at 4°C. The paired PCR tubes for each sample were then combined into single 1.5ml LoBind eppendorfs. Magic bead clean-up (as above) was performed, with 110 μ l magic beads (1.1X). The purified amplified DNA was eluted in 20 μ l 0.1X TE buffer and transferred to new LoBind tubes. D1000 high sensitivity screen tapes and 2200 TapeStation (Agilent, USA) were used to quantify libraries.

3.7 Pooling, denaturing and diluting libraries

Libraries were then denatured and diluted, following the NextSeq denature and dilute libraries guide, ready for sequencing.

3.8 Sequencing

Sequencing of the resultant libraries was performed on the NextSeq 500 (Illumina, USA) platform using a paired-end run, according to the manufacturer's instructions.

3.9 Phosphoproteomics

3.9.1 Collecting cell pellets

Greater than 20 million cells for each condition (in triplicate) was taken. The cell suspension was centrifuged at 1500g for five minutes. The supernatant was removed, the pellet was re-suspended in 500 μ l of ice-cold PBS, transferred to a 1.5ml eppendorf and centrifuged for a further five minutes. The supernatant was removed using a pipette and the pellet was stored at -80°C.

3.9.2 Cell lysis

300 μ l of fresh lysis buffer (10ml RIPA buffer, 3 μ l benzonase, 1 tablet phos stop) was added to each pellet, vortexed and left for 10 minutes on ice and then sonicated. The supernatant was transferred to a fresh tube.

3.9.3 Protein quantification

Protein concentrations were determined by BCA protein assay (Thermofisher, UK). 400 μ g of protein was taken from each sample. Samples were made up to a volume of 200 μ l with MilliQ-H₂O.

3.9.4 Protein Digestion

Kessler lab protocols were followed (<https://www.tdi.ox.ac.uk/research/research/tdi-mass-spectrometry-laboratory/mass-spectrometry/protocols-and-tools>). The lysed samples were reduced with 5 μ l of 200mM DTT in 0.1 M Tris buffer and incubated for 40 minutes at room temperature. The reduced samples were alkylated with 20 μ l of 200mM iodoacetamide in 0.1M Tris buffer, vortexed and then incubated for 45 minutes in the dark at room temperature. The protein was precipitated using methanol/chloroform extraction. The alkylated samples were transferred to 2ml eppendorfs. 600 μ l of methanol was added to each sample, followed by 150 μ l of chloroform and then vortexed gently. 450 μ l of MilliQ-H₂O was then added and vortexed gently. The samples were centrifuged at maximum speed on a table top centrifuge for one minute. The upper aqueous phase was removed, without disturbing the precipitate at the interface. 450 μ l of methanol was added to each sample, without disturbing the disc and centrifuged for two minutes. Protein pellets were resuspended, one sample at a time: the supernatant was removed and 100 μ l of 6M urea in 0.1M Tris buffer was added. The samples were vortexed and then sonicated (???). Samples were diluted with 500 μ l MilliQ-H₂O, to ensure the final urea concentration was below 1M. Porcine trypsin (Sequencing Grade Modified Trypsin; Promega, USA) was added in a 1:50 ratio of enzyme:total protein content of sample, such that 40 μ l

of trypsin solution containing 8µg trypsin in 0.1M Tris buffer was added to each sample. Samples were left to digest overnight at 37°C in an incubator shaker.

3.9.5 Peptide purification

The following day, the reaction was stopped, acidifying samples to 1% Trifluoroacetic acid (TFA). Samples were desalted and concentrated using 1ml C-18 Sep-Pak (Waters) cartridges. Two reagents were used: solution A (98% MilliQ-H₂O, 2% Acetonitrile (CH₃CN) and 0.1% TFA) for washing and solution B (65% Acetonitrile, 35% MilliQ-H₂O and 0.1% TFA) for activation and elution. The columns were flushed with 1ml of solution B and then washed with 1ml of solution A. The digested samples were added to the columns and vacuumed through slowly. Two 1ml washes with solution A were performed. Fresh, labelled eppendorfs were placed beneath the columns and peptides were eluted with 500µl of solution B. For phosphopeptide-enrichment, 90% of the peptides were removed for Immobilized Metal Affinity Chromatography (IMAC) on a Bravo Automated Liquid Handling Platform (Agilent). 10% of the peptides were used for total proteome analysis. Eluted peptides were dried using a vacuum concentrator (Speedvac, Eppendorf) and stored at -20°C until analysis by mass spectrometry (MS). Prior to MS analysis, dried peptides were resuspended in solution A.

3.10 Ubiquitinomics

3.10.1 Collecting cell pellets

100 million cells were taken for each condition in triplicate. The cell suspension was centrifuged at 1500g for five minutes. The supernatant was removed, the pellet was re-suspended in 500µl of ice-cold PBS and centrifuged for a further five minutes. The supernatant was removed and the pellet was stored at -80°C.

3.10.2 Cell lysis

PMTScan Ubiquitin Remnant Motif Kit (K-ε-GG; Cell signalling, USA) was used, following the manufacturer's protocol (REF). Pellets were solubilized and

denatured in 4ml urea lysis buffer (20mM HEPES, pH 8.0, 9M urea, 1mM sodium orthovanadate, 2.5mM sodium pyrophosphate, 1mM β -glycerophosphate). The lysates were sonicated on ice, with two bursts of 15 seconds with a one minute break in-between.

3.10.3 Protein quantification

Protein concentrations were determined by BCA protein assay (Thermofisher, UK). All samples were found to contain between 10mg and 20mg of protein, so all of the available protein was used, with no normalisation.

3.10.4 Protein digestion

Lysates were reduced using dithiothreitol (DTT) at a final concentration of 4.5 mM for 30 minutes at room temperature. The reduced samples were alkylated using iodoacetamide (100mM final) for 15 minutes in the dark at room temperature. The alkylated samples were diluted four-fold with 20mM HEPES (pH 8.0) and digested with 400 μ l trypsin solution, containing 1mg ml⁻¹ trypsin-TPCK (Worthington, LS003744) in 1mM HCl. Samples were left to digest overnight at room temperature on a rotator.

3.10.5 Peptide purification

The following day, the reaction was stopped, acidifying samples to 1% Trifluoroacetic acid (TFA). Samples were desalted and concentrated using 10ml C-18 Sep-Pak (Waters) cartridges. The columns were activated using 5ml of solution B, washed with 10ml of solution A. The samples were added to the columns and ran through slowly. The peptides were washed with 10ml of solution A. The cartridges were then removed from the vacuum and the peptides were eluted into fresh falcon tubes with 6ml of solution B, using the plunger of the syringes. 20 μ g of digested protein was removed from each sample for matching total proteome analysis. The eluate was kept at -80°C overnight. The frozen peptide solutions were lyophilized for two days and then stored at -80°C.

3.10.6 Immunoaffinity purification

10x immunoaffinity purification (IAP) buffer provided with PTMScan Kit was diluted to 1x concentration with MilliQ-H₂O. Purified peptides pellets were resuspended in 1.4ml of IAP buffer by pipetting up and down and transferred to 1.7ml eppendorfs. The samples were centrifuged at 4°C for 5 minutes at 10000xg and kept on ice whilst preparing antibody beads. The anti-body bead slurry was centrifuged (30 seconds at 2000 g) and 1ml of PBS was added and then centrifuged. The supernatant was removed and the antibody beads were washed a further four times with PBS and resuspended in 40μl of PBS. The peptide solution was transferred to the antibody vial and the solution was incubated on a rotator for two hours at 4°C. The samples were centrifuged, put on ice and the supernatant was removed. The beads were washed twice with 1ml IAP, followed by three washes with 1ml chilled HPLC water. Immunoprecipitated material was eluted at room temperature in 55μl and 50μl 0.15% TFA in water, letting the sample stand for 10 minutes after each elution, with gentle mixing every two-three minutes. The eluates were centrifuged and the supernatant was transferred to new tubes. Peptide material was desalted and concentrated using 1ml C-18 Sep-Pak cartridges as above. Prior to mass spectrometry analysis, purified GlyGly-modified peptide eluates and matching proteome material were dried by vacuum centrifugation, and re-suspended in solution A.

3.11 Liquid-chromatography-tandem mass spectrometry

Liquid-chromatography-tandem mass spectrometry (LC-MS/MS) analysis was performed using a Dionex Ultimate 3000 nano-ultra high pressure reverse-phase chromatography coupled on-line to an Orbitrap Fusion Lumos mass spectrometer (Thermo Scientific) (REF: adan's 3-5 dropbox). In brief, samples were separated on an EASY-Spray PepMap RSLC C18 column (500mm × 75μm, 2μm particle size; Thermo Scientific) over a 60 min (120 min in the case of the matching proteome) gradient of 2–35% acetonitrile in 5% dimethyl sulfoxide (DMSO), 0.1% formic

acid at 250nl min^{-1} . MS1 scans were acquired at a resolution of 60000 at m/z 200 and the top 12 most abundant precursor ions were selected for high collision dissociation (HCD) fragmentation.

3.12 CyTOF

Get data off ADAM

3.13 Data Processing

3.13.1 Bulk RNA-seq

Fasta files were processed using a CGAT-flow[111] pipeline, the workflow can be found at: https://github.com/cgat-developers/cgat-flow/blob/master/cgatpipelines/tools/pipeline_rnaseqdiffexpression.py. The pseudo-alignment tool, Kallisto[112], was implemented to pseudo-align reads to the reference human genome sequence (GRCh38 (hg38) assembly) and to construct a counts matrix of samples against transcripts. DESeq2[113] was used for differential expression analysis of counts matrices (using negative binomial generalized linear models) within the R statistical framework (v3.5.1). XGR[114], Reactome[115] and KEGG[116] were used to perform pathway analysis, within R. Org.Hs.eg.db[117], AnnotationDbi[118] and biomaRt[119] were used for converting between Ensembl IDs, HGNC symbols and ENTREZ IDs.

3.13.2 ATAC-seq

Raw ATAC reads (in fasta file format) were mapped to the GRCh38 reference genome using the CGAT-flow mapping pipeline (https://github.com/cgat-developers/cgat-flow/blob/master/cgatpipelines/tools/pipeline_mapping.py), using the mapper Bowtie. The mapped bam files were then used as input for the CGAT-flow peak calling pipeline ((https://github.com/cgat-developers/cgat-flow/blob/master/cgatpipelines/tools/pipeline_peakcalling.py)). Filtering was

performed to filter out [what is filterd out!!] and peak calling was implemented using macs2 (v2.2.7)[120].

3.13.3 Single-cell RNA-seq

The computational pipeline outlined in section 4.2 was used to process scRNA data.

3.13.4 LC-MS/MS

Mass-spectrometry raw data were searched against the UniProtKB human sequence data base and label-free quantitation (LFQ) was performed using MaxQuant Software (v1.5.5.1). Digestion was set to trypsin/P. Search parameters were set to include carbamidomethyl (C) as a fixed modification, oxidation (M), deamidation (NQ), and phosphorylation (STY) as variable modifications. A maximum of 2 missed cleavages were allowed for phosphoproteome analysis and 3 for the GlyGly peptidome analysis, with matching between runs. LFQ quantitation was performed using unique peptides only. Label-free interaction data analysis was performed using Perseus (v1.6.0.2). Results were exported to Microsoft Office Excel and imported into the R statistical framework (v3.5.1) for further analysis.

4

Computational workflow generation

4.1 Introduction

4.1.1 Reproducible workflows

In data analysis, particularly in bioinformatics, many users create simple bash or R scripts to execute the specific task at hand. However, if this is done often, the user can have an accumulation of these single-use scripts, which are often named uninformatively and never used again. Subsequently, the user may create scripts which perform the same function numerous times. Additionally, users may just use the command line alone to perform tasks. This means that exactly how they performed the analysis is difficult to find or not recorded. These are bad practices in terms of efficiency and reproducibility. It is much better practice to create well-documented, generalised workflows which can then be applied to multiple different experiments. This enables the user to reuse their code more easily and reproduce results, if need be. This also allows other researchers to reproduce results or apply the code to their own research.

In addition to creating generalised, reproducible workflows, it can be beneficial to create more extensive computational pipelines for jobs which require multiple tasks or actions to be performed sequentially.

4.1.2 Computational pipelines

A computational pipeline consists of a series of manipulations and transformations, where the output of one element is the input of the next. Often these elements are executed in parallel. Pipelining ‘omics’ data-processing means that tasks that are not interdependent can be executed simultaneously. Additionally, multiple samples can be processed in parallel, thereby reducing run time. There are many available pipelining frameworks, for example Snakemake[121], Luigi and Ruffus[122].

For this work, a series of computational pipelines and workflows were generated. Ruffus and CGAT-core[123] were used as the backbone for the pipelines developed.

4.2 scRNA-Seq pseudoalignment pipeline

Fewer pipelines exist for single-cell RNA-Seq compared to bulk RNA-Seq. For the Chromium 10X Genomics platform, most of the processing and analysis is automated by Cell Ranger; however for other technologies, the workflow is not as well defined. A single-cell analysis pipeline was constructed with the aim to produce an easy-to-use, robust and reproducible workflow that works for Drop-Seq as well as 10X technology, which utilises pseudoalignment rather than traditional mapping methods.

4.2.1 Psuedoaligment

Traditional mapping techniques such as Tophat[124] or STAR[125], rely on aligning each read to a reference genome. This is generally very time consuming and computationally expensive. Another challenge that arises with traditional mapping is the occurrence of multi-mapping, whereby a read cannot be uniquely aligned as it could map equally well to multiple sites in the genome[126]. More recently, a series of methods called pseudoaligners have been developed that overcome some of the issues associated with traditional mapping approaches. Pseudoalignment (sometimes referred to as quasi-mapping) methods provide a lightweight, alignment-free alternative to traditional mapping. It has been shown that information on where exactly inside transcripts sequencing reads may have originated is not required for

accurate quantification of transcript abundances[127]. Rather, only which transcript the read could have originated from is needed and transcript abundances are calculated by computing the compatibility of reads with different transcripts. This negates the need for alignment to a reference genome, alleviating the issue of multi-mapping and reducing the computational load. Pseudoaligners have been shown to complete data processing of RNA-seq datasets up to 250-times faster than traditional alignment and quantification approaches[112]. Kallisto[112] and Salmon[128] are tools which implement pseudoalignment. They have similar speed and accuracy for bulk RNA-seq data¹.

Pseudoalignment of scRNA-seq

Pseudoalignment tools have recently been developed for droplet-based scRNA-seq analysis (dscRNA-seq). Additional challenges come with dscRNA-seq data processing, having the extra complication of cellular barcodes (CBs) and unique molecular identifiers (UMIs). These tools must handle transcript abundance estimation, as with bulk RNA-seq analysis, but also perform CB detection, collapsing of UMIs (arising from PCR duplication of molecules) and barcode error correction. Kallisto BUS[129] has been developed as an analysis tool and file format specifically for single-cell analysis, alongside BUStools, for processing of the resultant BUS file[130]. Salmon Alevin[131] has also been developed for single-cell RNA-seq analysis.

Pipeline outline

Kallisto BUS or Salmon Alevin performs pseudoalignment and generation of a cell-by-gene expression counts matrix. Quality control is performed using Scater[132] and alevinQC. Clustering is performed using Seurat3[133] and Monocle[134]. Clusters are projected onto tSNE and UMAP plots. Differentially expressed genes are identified by performing non-parametric Wilcoxon tests on $\log_2 TPM$ expression values and Fisher's exact test for comparing expressing cell frequency, these p values combined using Fisher's method. Multiple comparisons are accounted for by performing the Benjamini-Hochberg correction to adjust the false discovery rate.

¹<https://liorpachter.wordpress.com/2017/09/02/a-rebuttal/>

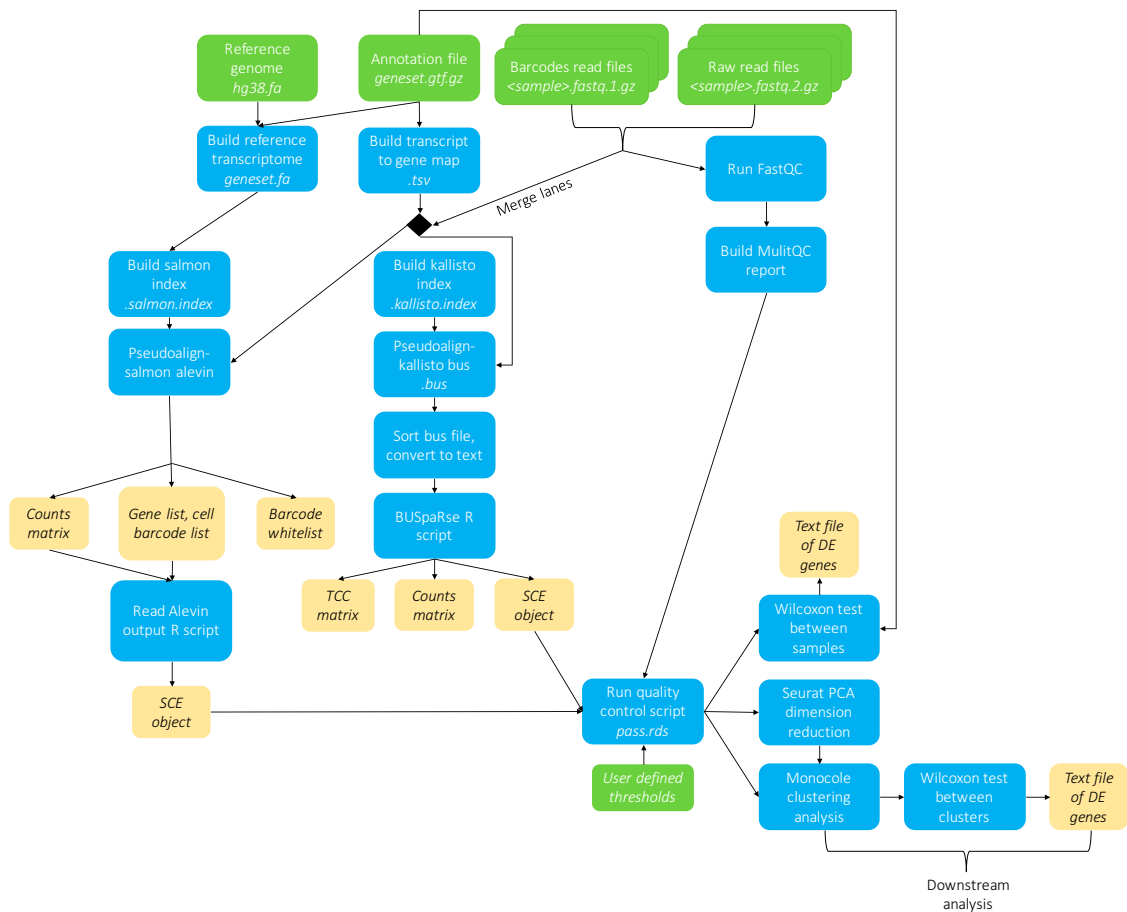


Figure 4.1: Flowchart outlining scRNA-Seq pseudoalignment pipeline- PLACEHOLDER- remake figure

4.2.2 Benchmark

Benchmarking measures the performance of a method/software relative to other methods available. Run time and the accuracy of results are often the factors considered in a benchmark. To be able to calculate the accuracy of results, the ‘true’ results must be known. This is difficult in scRNA-seq analysis as no gold standard analysis protocol exists. Instead, methods are compared against simulated results which act as the underlying ‘ground truth’.

Simulated data

Simulated reads with a know ground truth counts matrix were generated as follows: 10X (version 2) fastq files of 4k PBMCs from a healthy human donor

were downloaded ². These sequencing files were processed using Salmon Alevin. The resulting Alevin output folder was used as input for Minnow, using Minnow's alevin-mode. Minnow generates droplet-based scRNA-seq simulated reads, working backwards from a known counts matrix to generating raw sequencing files from which the counts matrix could have originated. The valid cell barcode list (whitelist) for 10X chemistry was used (*737K-august-2016.txt*³). Minnow was ran with an error rate of 0.001 and with 12 simulated PCR cycles. Minnow accounts for core experimental dscRNA-seq characteristics, such as PCR amplification bias, barcode sequencing errors, the presence of doublets and ambiguously mapped reads, to try and emulate a realistic set of sequencing reads consistent with the provided counts matrix.

The ground-truth counts matrix was converted to a Single Cell Experiment object (SCE) and the simulated reads were used as input for the scRNA-Seq pseudoalignment pipeline. The resulting count matrices outputted by Salmon Alevin and Kallisto BUS were converted into SCEs, subset and reordered so that they all contained the same cells and genes, in the same order. The Salmon Alevin and Kallisto BUS produced SCEs could then be compared to the ground truth SCE.

Run time

The simulated reads consisted of 434 million reads. Running Salmon Alevin and creating an SCE object took approximately 64 minutes; running Kallisto BUS, sorting and creating an SCE object took approximately 24 minutes. Using the bustools 'count' command to create a counts matrix may have further reduced run time, however more time would be needed to parse it into R and create an SCE object.

Cell barcode handling

The ground-truth data contained 4340 cells. Alevin determined a threshold for the initial whitelist (a set of CBs that likely represent non-empty droplets) by finding a

²<https://support.10xgenomics.com/single-cell-gene-expression/datasets>

³<https://github.com/COMBINE-lab/minnow/blob/master/data/737K-august-2016.txt>

'knee' in the knee plot shown in Figure 4.2. This initial whitelist contained 5261 cell barcodes, each observed at least 191 times. Following barcode error correction, the final whitelist contained 4340 cells, all of which corresponded to the same CBs as the ground-truth data.

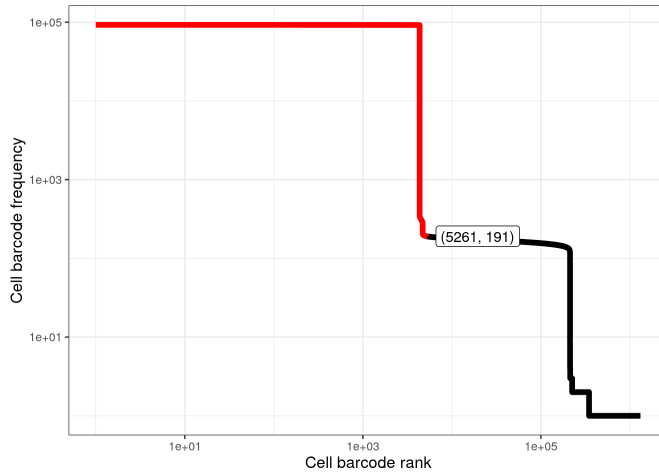


Figure 4.2: Alevin knee plot. This plot displays the number of times each cell barcode is observed, in decreasing order. Finding a 'knee' in this plot determines a threshold for the initial whitelist of CBs, which are unlikely to be empty droplets.

For Kallisto BUS, valid cell barcodes were determined using either emptyDrops (DropletUtils) or by using barcodeRanks and calculating the inflection point of a rotated knee plot (where the x- and y- axis are transposed; Figure 4.3). The inflection point method, gave a whitelist of 4339 cell barcodes (one fewer than the ground truth number), but all 4339 CBs corresponded to ground truth CBs. emptyDrops gave a total cell number of 12037, only 3746 of which were in the ground truth list of 4340 CBs. This was a large overestimate of number of cells present and the whitelist did not contain all of the valid CBs. Therefore, using the inflection point of the rotated knee plot was found to be the preferred method of filtering cell barcodes.

Gene expression predictive accuracy

To quantify each tool's accuracy of gene expression, precision, recall and an F1 score were calculated for each gene. The F1 score is a measure of a test's accuracy,

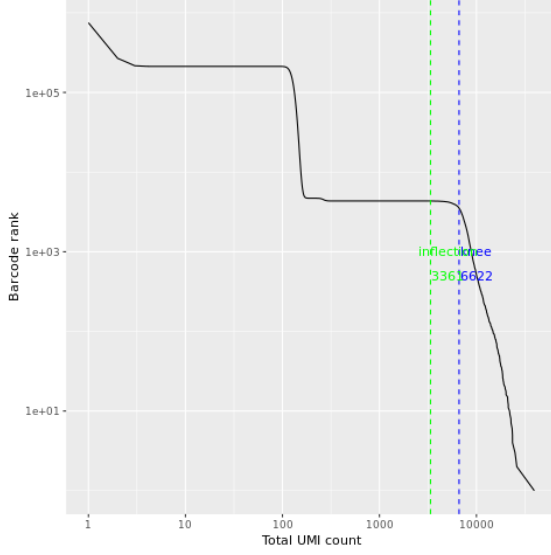


Figure 4.3: Kallisto BUS rotated knee plot. This plot shows the number of distinct UMIs against the rank of the barcode. The Pachter lab transpose the x- and y-axis on their knee plot, so that the x-axis displays distinct UMIs and the y-axis displays ranked cell barcodes, according to the number of corresponding UMIs to each CB. This is supposed to be more intuitive, having the number of distinct UMIs as the independent variable rather than cell barcode rank, as number of UMIs determine the cell barcode rank.

it is the harmonic mean of precision and recall:

$$\begin{aligned} \text{precision} &= \frac{tp}{tp + fp} \\ \text{recall} &= \frac{tp}{tp + fn} \\ F_1 &= 2 \cdot \frac{\text{precision} \cdot \text{recall}}{\text{precision} + \text{recall}} \end{aligned} \tag{4.1}$$

Where for each gene: tp = number of true positives, fp = number of false positives, fn = number of false negatives.

		Ground truth	
		Expressed	Not Expressed
Alevin /BUS	Expressed	True positive	False positive
	Not Expressed	False negative	True negative

Table 4.1: Carol diagram of true/false positives/negatives based on expression between predicted values by Alevin/BUS and the ground truth matrix.

No expression was denoted by 0, and expression by 1. When recall or precision

was undefined, i.e. a gene in Alevin/BUS matrix or the ground-truth matrix was not expressed by any cell, F score was defined as 0.

The mean F1 scores for Alevin and BUS processed data (Figure 4.4) were extremely similar to each other with scores of 0.93 and 0.95, this was due to the large number of F1 scores equal to 1. Figure 4.5 shows the distribution of F1 scores more clearly. Alevin seemed to produce more lower F1 scores than BUS.

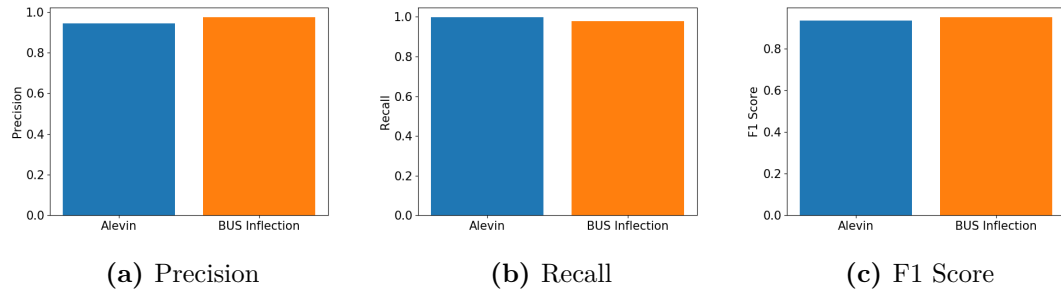


Figure 4.4: F1 score. Two times the product of precision and recall divided by the sum of precision and recall. Measure of accuracy for the tools ability to predict gene expression. Expression classified by 0 or 1. Undefined scores have been removed. F1 scores were calculated for each gene across each cell.

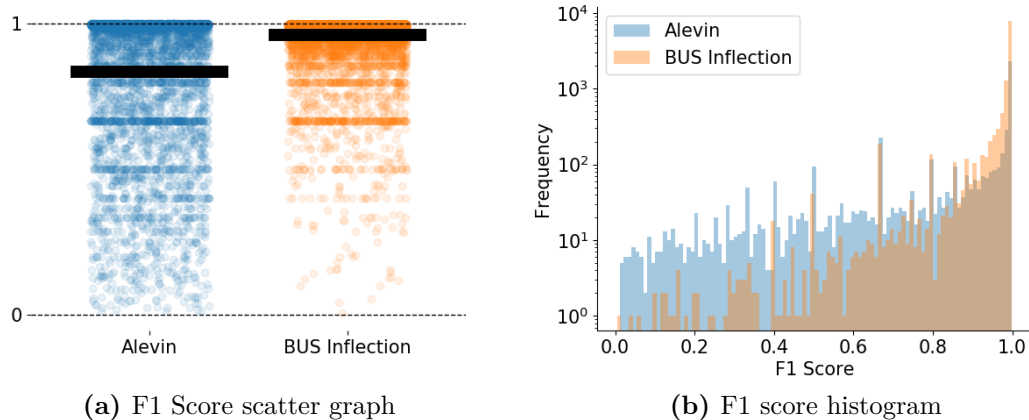


Figure 4.5: F1 score distributions. 4.5a shows the F1 score for each gene expressed across all 4339 cells. The black bar denotes the mean F1 score for each cell. F1 scores of 0 have been removed.

Clustering

Clustering analysis was performed to visualise how well the tools processed the single-cell data and how clusters compared to ground-truth data. Seurat3 integrative

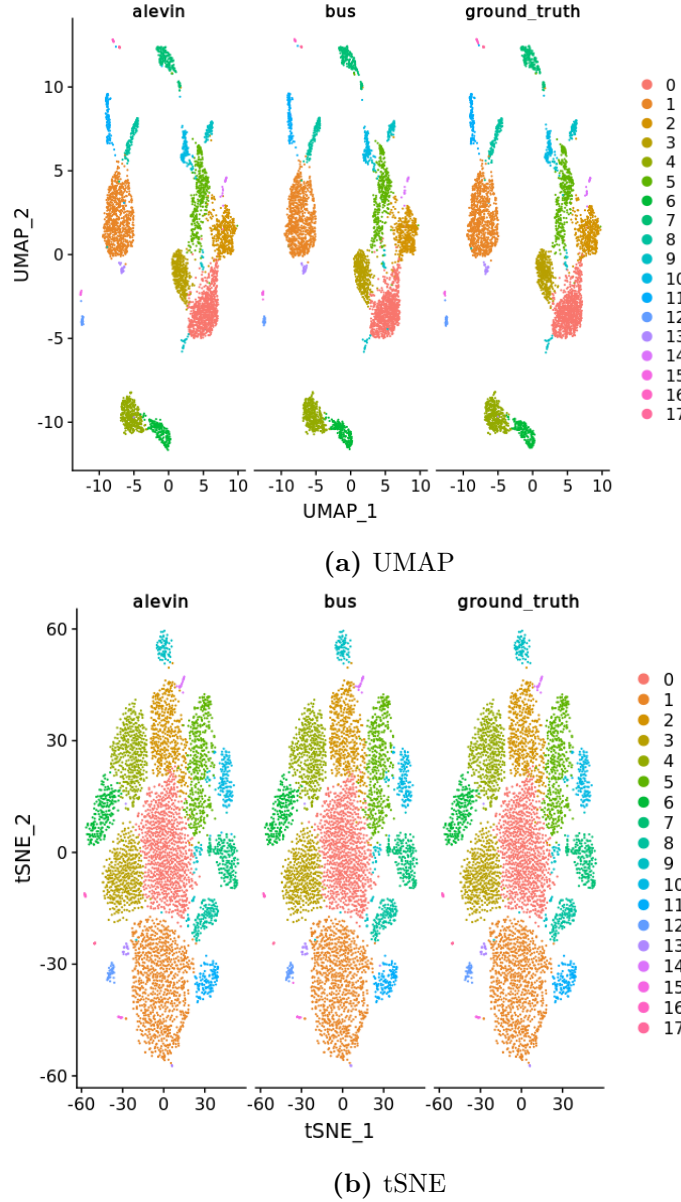


Figure 4.6: Clustering analysis of the simulated data. 18 clusters are present in the ground truth data and Alevin and BUS processed data. Integrated clustering was performed using Seruat3[133], using both Uniform Manifold Approximation and Projection (UMAP) and t-distributed Stochastic Neighbor Embedding (tSNE) dimension reduction techniques.

analysis was performed so that the clusters of each sample could be directly compared. Figure 4.6 shows clustering of Alevin, BUS and ground-truth clustered data, using UMAP and tSNE dimension reductions. 18 clusters are present in all three of the data sets. Visual analysis suggests that the two dscRNA-seq quantification tools compare well to the ground-truth and capture most aspects of the data. From the

benchmark it seems as if both tools are fit for purpose and can accurately quantify gene expression and correctly handle CBs and UMIs.

4.3 Updated scRNA-seq pipeline

Following the bench-mark it was decided that Kallisto BUS and BUStools would be used to analyse single-cell data. This was due to its faster run-time and higher F1 scores. The analysis pipeline has been updated continually throughout the project.

4.4 scRNA-Seq velocity analysis pipeline

4.4.1 RNA velocity

"RNA velocity is a high-dimensional vector that predicts the future state of individual cells on a timescale of hours"[135]. In combination with clustering analysis, the trajectory of a single-cell can be tracked.

4.5 ATAC-seq analysis pipeline

4.6 tRNA-seq analysis pipeline

5

Bulk RNA-seq analysis of PRS inhibitors

5.1 Introduction

Although MM treatment has improved significantly in the last 10-20 years, MM remains an incurable disease. Most MM patients relapse and become resistant to drugs they have previously been treated with. Therefore, research into novel therapeutics that can overcome multi-drug resistance and can be used to treat relapsed patients is of great importance. A new exciting class of compounds in treating MM have been derived from Febrifugine. Febrifugine was first isolated from the Chinese herb *Dichroa febrifuga*, considered an important herb in traditional Chinese medicine, shown to have antimalarial effects. One such derivative, Halofuginone, has been shown to inhibit T Helper 17 (TH17) cell differentiation, by activating the amino acid response (AAR)[73]. Halofuginone inhibits the enzyme glutamyl-prolyl tRNA synthetase (EPRS). EPRS is a bifunctional aminoacyl-tRNA synthetase (AARS) and catalyses the aminoacylation of glutamic acid and proline tRNA species (i.e. it charges tRNAs with glutamic acid and proline). Halofuginone and Febrifugine compete with proline at the prolyl-tRNA synthetase active site of EPRS, specifically targeting utilisation of proline during translation[74]. This results in an accumulation of uncharged prolyl-tRNAs, giving the same cellular environment as if the cell were proline deficient, triggering the AAR to respond to the apparent proline deprived state.

AARSs are essential in protein synthesis, aiding in building chains of amino acids. Human cancer cells often have an increased rate of protein synthesis, this is especially true in multiple myeloma, creating huge amounts of non-functional paraproteins, therefore more reliant on AARSs. This is why MM was thought of as a good candidate for AARS inhibitor treatment. Previously, Halofuginone (HF) has shown anti-MM activity in vitro and in-vivo. HF induced cytotoxicity and apoptosis in numerous MM cell-lines and primary MM cells. HF was also shown to inhibit MM growth and prolong survival in a mouse xenograft MM model[109].

However, it has been shown that HF's anti-MM effect can be reduced in the presence of excessive proline. Additionally, tumours have more proline than healthy cells <REF>. This means that HF has a very narrow therapeutic window. Recently, The Mazitschek group have synthesized numerous other compounds which also target the PRS site of EPRS. One such example, coined NCP26, binds to the ATP binding site of PRS and does not compete with proline for the proline site of PRS. More PRS inhibitors have been synthesized by the group, including MAZ1805 (Halofuginol) and NCP22.

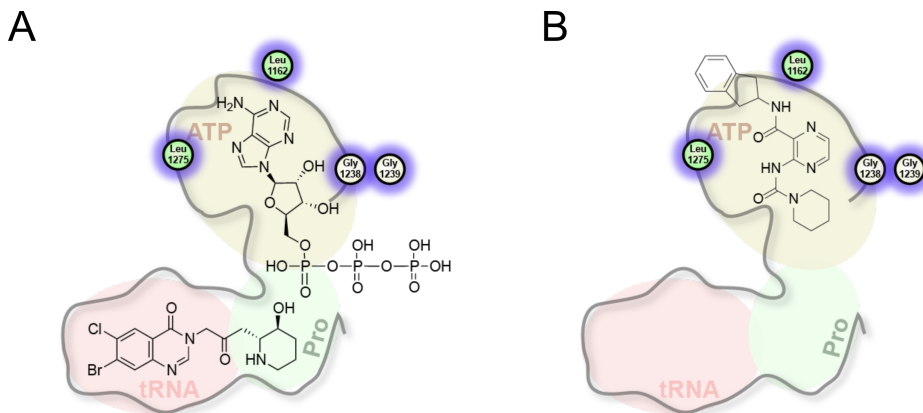


Figure 5.1: Figure by Ralph Mazitschek, kindly agreed (GET PERMISSION). The structures of Halofuginone/MAZ1392 (A) and NCP26 (B). Halofuginone is ATP dependent, proline and tRNA competitive. NCP26 is ATP competitive and proline uncompetitive.

5.2 Results

5.2.1 Dose response curves

The effect of the PRS inhibitors (NCP22, NCP26, Halofuginol and Halofuginone) on MM cell viability was investigated using the MM cell lines: AMO-1 and CFZ-R L363.

5.2.2 Synergy with existing MM treatment

5.2.3 Bulk RNA-seq

5.2.4 Experiment overview

The treatment of drug sensitive and carfilzomib resistant MM cell-lines with four compounds that inhibit the prolyl-tRNA synthetase active site of EPRS was investigated using bulk RNA-seq. PI-sensitive WT AMO-1 cells and carfilzomib resistant L363 cells (check batch 1 type- are they L363 or AMO-1) were treated with 1 μ M of MAZ1392 (Halofuginone), NCP26, NCP22 and MAZ1805 or a DMSO control or 100nM Carfilzomib (WT cells only) for 6 and 24 hours.

5.2.5 Effect of carfilzomib on WT cells

5.2.6 WT AMO-1 cells

5.2.7 Carfilzomib resistant cells

5.2.8 Amino acid starvation response

6

Single-cell RNA-seq analysis of PRS inhibitors

6.1 Introduction

MM cells grow within the bone marrow and are supported as they grow by their microenvironment. The MM microenvironment comprises a cellular compartment (composed of immune cells, endothelial cells, osteoblasts, osteoclasts and stromal cells) and a non-cellular compartment (composed of the extracellular matrix (ECM), cytokines, chemokines and growth factors)[136, 137]. There are interactions between malignant plasma cells and the surrounding microenvironment. The bone marrow microenvironment has been indicated to play a supportive role in migration, proliferation, differentiation and drug resistance of malignant plasma cells. There is evidence linking the tumour microenvironment to progression of MGUS to active MM, for example significant matrix remodelling has been seen between the bone marrow of healthy individuals, MGUS and MM patients[137]. Therefore, to get an accurate picture of MM, information must be acquired about the surrounding niche.

Historically, the tumour environment has been investigated following the isolation of populations of cells sorted from the tumour and then sequenced using traditional microarray or bulk RNA-seq techniques. Bulk techniques measure the average expression across a sample, which is the sum of cell type specific expression weighted by cell type proportions. Single-cell techniques measure expression for each individual cell and therefore provide information on clonal diversity that may

be lost when pooling cells into bulk samples. Furthermore, multiple myeloma is an extremely heterogeneous disease, this is seen both between patients and within an individual's own tissue. Applying single-cell techniques to capture the inter- and intra-individual heterogeneity is fundamental to identifying molecular and cellular signatures that define MM.

The advent of single-cell technologies has led to a better understanding of the complexity and diversity of the tumour microenvironment. Seminal papers from Melnekoff et al. (2017)[138] and Ledergor et al. (2018)[139] use scRNA-seq to reveal clonal transcriptomic heterogeneity in MM samples. Melnekoff et al. (2017) demonstrated the clonal heterogeneity within MM using samples that were collected from eight relapsed MM patients. The group performed t-SNE clustering analysis and the samples separated into eight transcriptionally distinct clones, each corresponding to a different patient. This highlights the inter-patient differences of MM. Ledergor et al. (2018) performed a similar study to evaluate clonal heterogeneity within MM but also had a set of controls with which to compare the MM group. They found that MM patients have greater inter-individual transcriptional variation, where each MM patient possessed a unique and individual plasma cell transcriptional program. They also showed substantial intra-tumour heterogeneity (subclonal structures) of plasma cells in a third of their MM patient cohort. These papers established the importance of using single-cell techniques to study MM, as to not miss the underlying clonal heterogeneity. However both of these papers focussed solely on plasma cells and did not look at the surrounding bone marrow microenvironment. To truly understand the complexities of MM and treatment of MM, interactions between plasma cells and the bone marrow niche must also be explored using single-cell techniques.

6.1.1 Experiment overviews

Three single-cell experiments, comprising samples from four MM patients, were performed to explore the effect of various compounds (including Halofuginone and NCP26) on MM patient tissue. The BM samples for experiments 1 and 2 were obtained from two treatment-naive, newly-diagnosed MM patients. Experiment

3 comprised samples from two patients, both with relapsed MM, therefore both presenting with a degree of acquired anti-cancer drug resistance. For experiment 1, BM samples were treated for 24 hours with 1 μ M Casin, GSK-J4, Halofuginone, NCP26, SGC-GAK, Verteporfin or a DMSO control, totalling 7 samples. For experiment 2, BM samples were treated with 1 μ M CAMKK2, CLK or CSNK2 for 24 hours; 1 μ M SGC-GAK, Halofuginone, NCP26 or a DMSO control for 24 and 48 hours, totalling 11 samples. For experiment 3, BM samples from patient 3 and 4 were treated for 24 hours with either a DMSO control, 1 μ M Halofuginone, 1 μ M NCP26 or 5 μ M NCP26, totalling 8 samples.

Following compound treatment, single-cell RNA-seq library preparation was performed by Dr Martin Philpott using the Chromium Next GEM Single Cell 3' GEM, Library and Gel Bead Kit v3.1 according to the manufacturer's instructions. Indexed libraries were quantitated by TapeStation, pooled and sequenced on an Illumina NovaSeq 6000 (Novogene, UK).

<GENEWIZ experiment 3 >

6.2 Data processing

Initially all four patient samples were processed and integrated together. However, integration was found to be poor between treatment naive patients and the relapsed patients. This was expected as MM patients' transcriptome has been shown to change considerably following <XYZ> rounds of treatments REF. Therefore, samples from experiments 1 and 2 (treatment naive patients 1 and 2) were integrated together and samples from experiment 3 (relapsed patients 3 and 4) were integrated together.

Experiments 1 and 2 contained treatment samples that were not of interest to this project. However, all samples originated from MM patients, therefore all 18 samples were included in the analysis up to and including the integration and annotation stage of data processing. This was to increase the granularity of the data, and allow for easier annotation of clusters. Downstream analysis in this work only includes DMSO, Halofuginone or NCP26 treated samples.

6.2.1 Analysis overview

The single cell analysis pipeline outlined in section <ENTER section> was used to process the data. Kallisto BUS/ BUStools was used to pseudoalign reads and quantify gene expression. Next, quality control and filtering of the samples was performed. Poor quality cells are likely to have a low number of genes and UMIs per cell. Any cells with fewer than 500 UMIs were removed. Cells with a gene count below 300 or above 6000 were removed. Cells with a mitochondrial ratio higher than 0.1 were removed (a high proportion of mitochondrial genes indicates mitochondrial contamination from dead or dying cells). After quality control and filtering of the data, clustering was performed using Seurat v3, followed by integration of all samples, using Seurat v3 and Harmony. The two experiments were too large to integrate across all samples using the Seurat SCTransform normalisation method, therefore a reference-based approach was taken, whereby a subset of samples were selected (based on their cell richness and relevance to the research question) and listed as ‘reference datasets’ for SCTransform normalisation. Harmony integration was also implemented, using patient and experiment as additional covariates.

Cell type annotation was performed by using several automated packages (singleR, clustifyr and scClassify), then by fine-tuning manually using a list of known biological markers. The HumanCellAtlas database was used to inform singleR and clustifyr annotation. scClassify was performed using a pre-trained scClassify model, based on seven PBMC single-cell datasets (including 10X V2, 10X V3, smartSeq, celSeq, dropSeq and inDrops datasets). As the reference datasets were based on healthy tissue, they are unable to label pathological cells, like myeloma cells. Myeloma cells were identified manually using a range of known markers, for example: CD38, CD138, SLAMF7 and BCMA (see table 6.2).

Experiment 2 was found to have an extremely high erythrocyte population (figure 6.1A and B). In addition, many other cell populations were expressing erythrocyte specific genes, where we would not expect to see them being expressed, for example MM cells expressing numerous haemoglobin subunit genes. Many of the variable features that Seurat uses for clustering analysis and dimension reduction were made

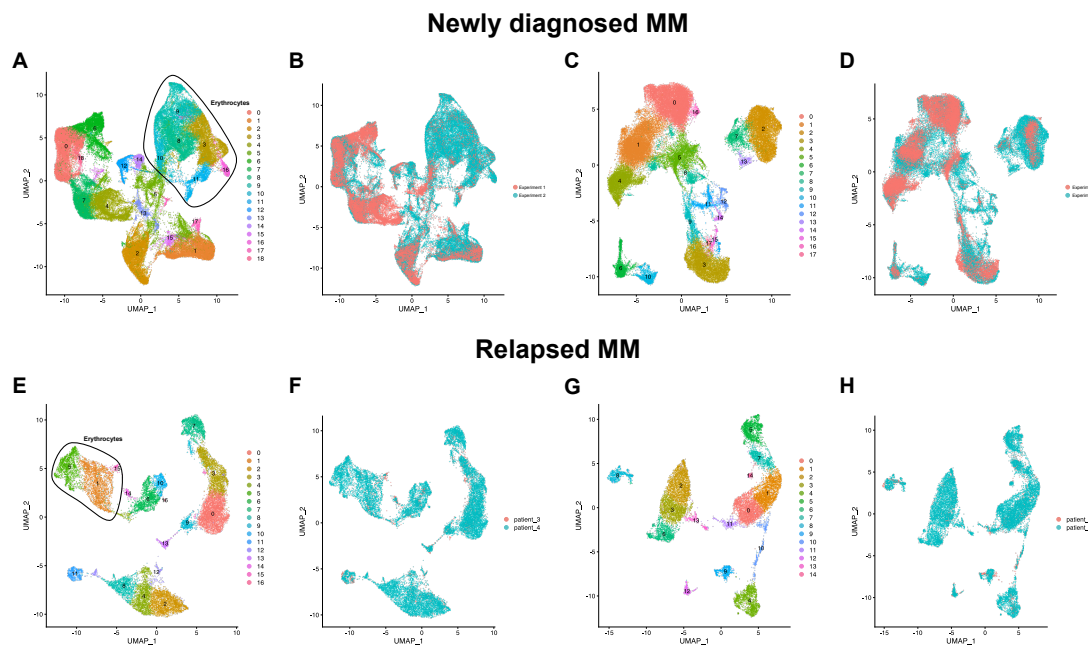


Figure 6.1: UMAP dimension plots following integration of samples from experiment 1 and 2 (treatment naive patients), and samples from patients 3 and 4 in experiment 3 (relapsed MM). [A-D] Experiment 1 and 2-newly diagnosed MM patients. [E-H] Experiment 3, patients 3 and 4- relapsed MM patients. [A, B, E, F] Integrated UMAP plots before erythrocyte cell and gene removal. Erythrocyte clusters are circled in A) and E). [C, D, G, H] UMAP plots following removal of erythrocyte cell clusters and genes and re-integration of samples. [B, D, F, H] show the composition of each dataset by experiment or patient.

up of these erythrocyte-specific and haemoglobin genes. The high expression of these genes was thought to be affecting the integration of the two experiments together. A theory for the presence of the large number of erythrocytes and un-localised erythrocyte gene expression is that perhaps the BM sample taken for experiment 2 was one of the later samples taken from the patient and contained a large amount of blood. Library prep clean-up may have missed many of these cells, leading to ambient erythrocyte RNA being present within many droplets.

It was decided to remove the erythrocyte clusters (clusters 3, 8, 9, 10, 11 and 16 in newly diagnosed; clusters 1, 5 and 15 in relapsed) and haemoglobin related genes or erythrocyte specific genes that seemed to be dominating expression in the integrated dataset. After the integrated Seurat object had the erythrocyte genes and cells removed, it was split back up into separate Seurat objects for each sample, and integration and clustering was performed again. Seurat's SCTransform with reference

Experiment	Patient	Total cells	Cells passing filter	Cell number after erythrocyte removal
Experiment 1	Patient 1	112452	25779	23915
Experiment 2	Patient 2	462560	61059	37161
Experiment 3	Patient 3	4894	2625	2257
	Patient 4	21682	18674	14934

Table 6.1: Total cells, the number of cells passing filter, and the number of cells passing filter once erythrocyte clusters were removed across all samples for each patient.

datasets and Harmony (using a multi-covariate model, accounting for each different sample and the two different experiments) were used to re-integrate all samples. Harmony integration was found to integrate clusters across patients and experiments better than using Seurat’s SCTransform. The Harmony integrated datasets were taken forwards and used for cell type annotation. Better integration was achieved after removing erythrocytes and erythrocyte-specific genes (see figure 6.1D).

A large erythrocyte component was also found for patient 4 for in experiment 3 (figure 6.1E and F). The same analysis workflow was applied to experiment 3, removing the erythrocyte cluster and erythrocyte specific genes and re-integrating using Harmony with samples and patients as covariates.

6.2.2 Annotation of re-integrated data

R packages clustifyr and scClassify were used to aid in cell type annotation of the integrated datasets, the result of this annotation can be seen in figure 6.2. Because healthy tissue datasets were used as references, the myeloma cluster could not be identified using these packages with these references alone. Both packages either incorrectly labelled the MM cell cluster as B cells, or were unable to assign any cell type to the myeloma cluster with any confidence and left it unassigned. However, the packages do give a good starting point for more detailed manual annotation using known biological markers.

Figures 6.3 and 6.4 show how the MM cell clusters were identified. From MM cells, you would expect to see expression of CD38, but lower expression than in normal plasma cells. You would expect to see high expression of the pathological

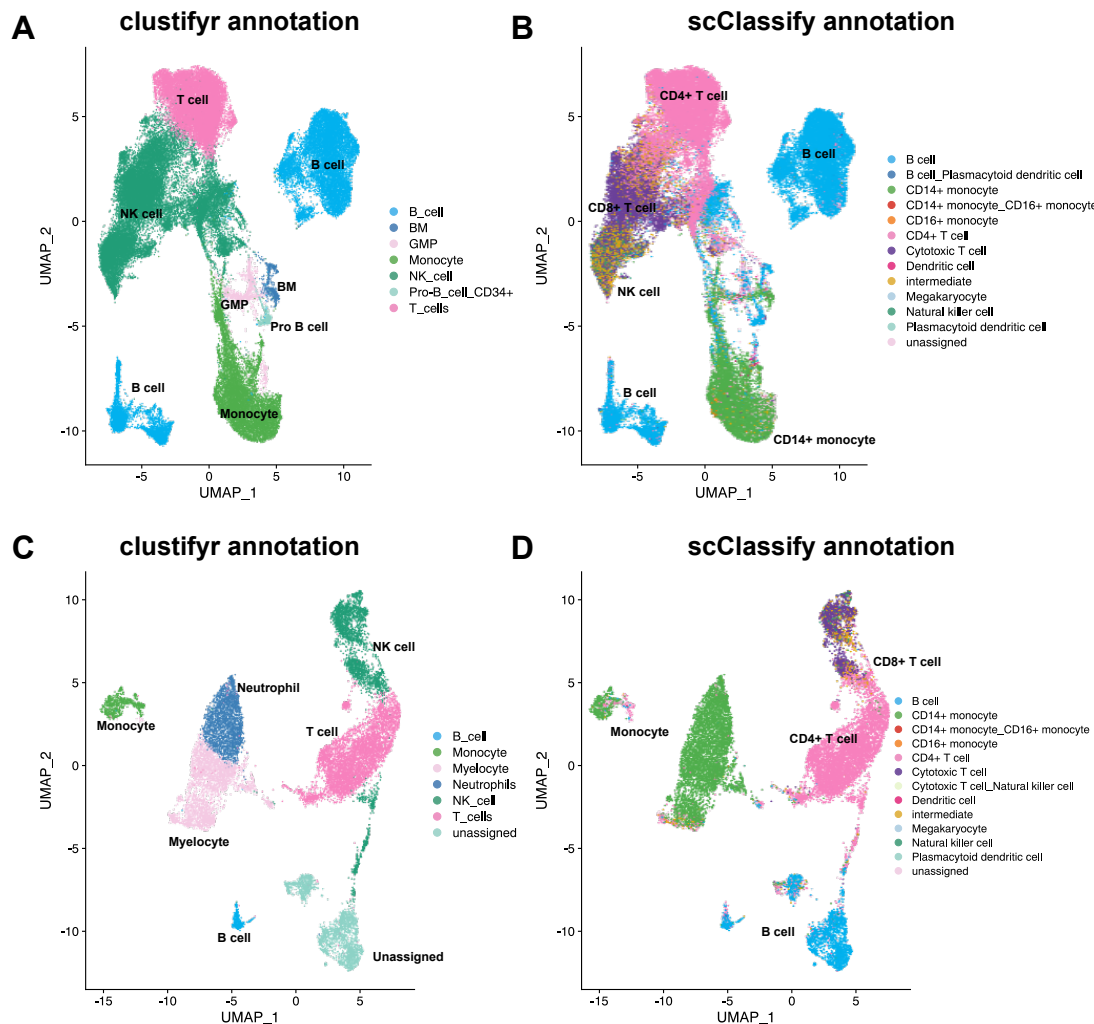


Figure 6.2: Automated annotation of MM cell clusters, using the R packages clustifyr and scClassify in combination with reference datasets. [A, B] newly diagnosed MM, [C, D] relapsed MM patients. The output of automated packages clustifyr and scClassify used to aid cell type annotation. Clustifyr assigns a cell type to each cluster of cells, scClassify assigns a cell type to each individual cell (labels have been added post-hoc). Clustifyr was used in conjunction with the HumanCellAtlas reference, and scClassify was ran with a pretrained model trained on seven PBMC single cell RNA-seq datasets. Both references are from healthy datasets so neither are able to identify the myeloma cell population.

marker CD138 in MM cells, as well as high expression of SLAMF7, BCMA, KRAS, IGKC and IGL2, however these are not exclusive to the MM cluster. You would expect to see little or no expression of CD45 and CD19 in the MM cluster and reduced expression of CD20 in MM cells compared to normal B cells. Using the expression of these markers, clusters 2, 7 and 13 were identified as the MM cell population in the newly diagnosed dataset; and cluster 4 was identified as the

MM cell population in the relapsed MM dataset.

Cell type	Expressed/ over-expressed	Not expressed/ reduced expression
Multiple myeloma cells	CD38, CD138, SLAMF7, BCMA, KRAS, IGKC, IGCL2	CD20, CD19, CD45 ?
Normal plasma cells	pc place holder	place
B cells	CD38	b down
CD4+ T cells	CCR7, SELL, TCF7, TRAC*, CD3D*	cd4 down
CD8+ T cells	CD8A, TRAC*, CD3D*, GZMH+, GZMB+, GZMA+, PRF1+	cd 8 down
NK cells	KLRB1, KLRF1, GZMH+, GZMB+, GZMA+, PRF1+	nk down
Dendritic cells	dc up	dc down
Monocytes	mono up	mono down
etc...	else	else down

Table 6.2: Manual annotation markers for cell types originating from transcriptomic profiles of bone marrow samples. * = General T cell markers, + = Cytotoxic markers

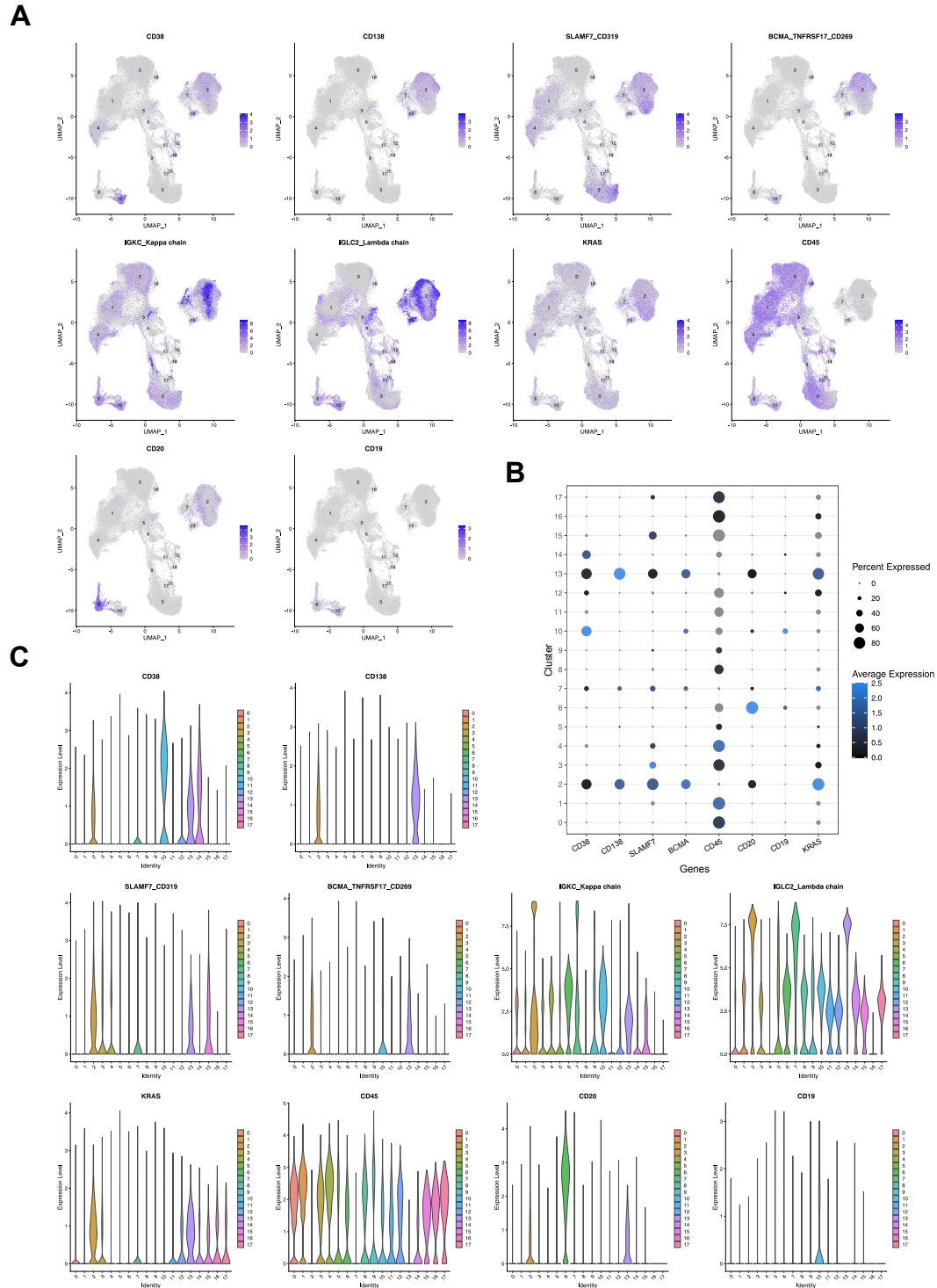


Figure 6.3: Manual annotation of MM cell clusters in experiment 1 and 2 (newly diagnosed MM) using known MM biological markers. A) Seurat UMAP feature plots showing expression for MM markers. Purple indicates expression of the corresponding gene by a cell. B) A dot plot showing the percentage of cells in a cluster expressing a given gene, and the average expression of that gene for the cluster. C) Violin plots for each cluster and expression levels for each marker listed above.

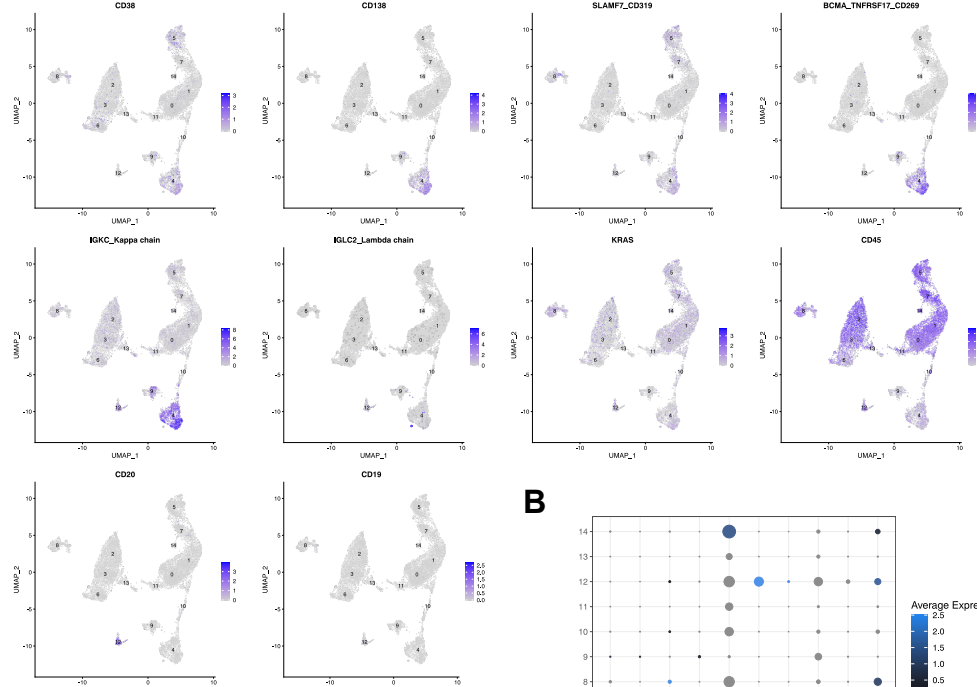
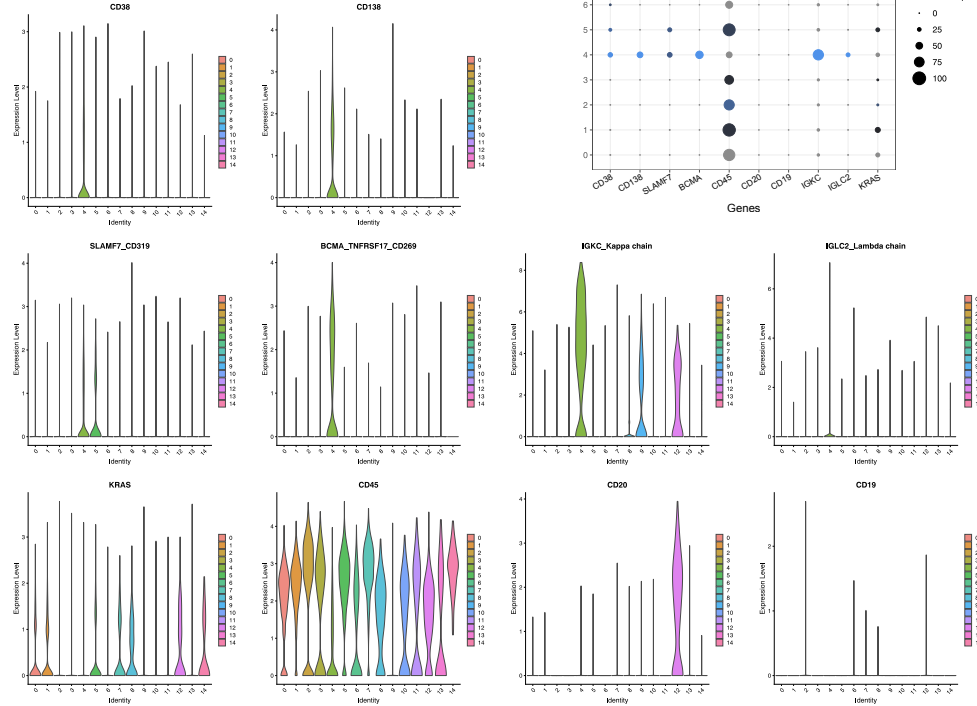
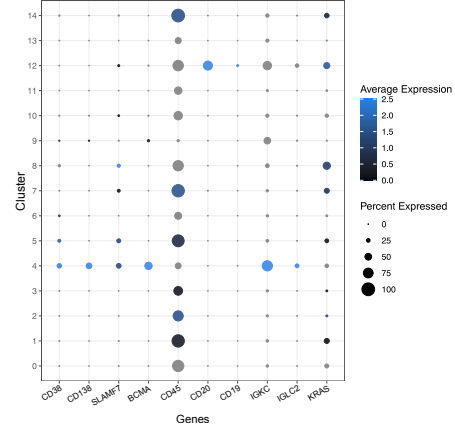
A**C****B**

Figure 6.4: Manual annotation of MM cell clusters in experiment 3 (relapsed MM) using known biological markers A) Seurat UMAP feature plots showing expression for MM markers. Purple indicates expression of the corresponding gene by a cell. B) A dot plot showing the percentage of cells in a cluster expressing a given gene, and the average expression of that gene for the cluster. C) Violin plots for each cluster and expression levels for each marker listed above.

6.3 Results

6.3.1 Newly diagnosed MM

Composition

Cluster composition is shown in figures 6.5. Large number of cells were killed by Halofuginone treatment at both 24 and 48 hours. Clusters 0, 1 and 5 (T-cells, monocytes and MM cells) seem particularly affected.

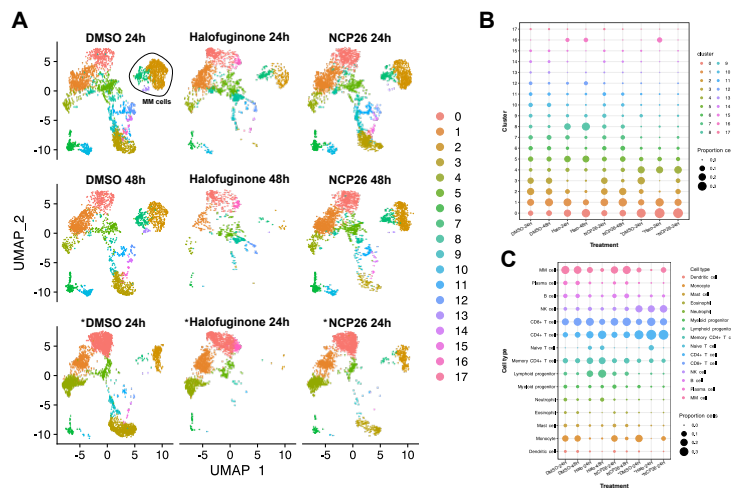


Figure 6.5: Composition analysis of newly diagnosed MM. A) UMAP cell composition plots separated by treatment condition. B) Dot plot showing proportion of cells in each cluster for each sample. C) Dot plot showing proportion of cells in each cell class for each sample (as labelled in Figure <XYZ>). * indicates samples originating from experiment 1, no star indicates an experiment 2 origin.

Differential expression

6.3.2 Relapsed MM

6.4 Myeloma bone marrow classifier

7

tRNA-seq analysis of PRS inhibitors

7.1 Introduction

7.1.1 Experiment overview

In parallel with mRNAs

7.2 Data processing

7.2.1 Quality control and filtering

7.3 Results

7.3.1 tRNA results

7.3.2 mRNA results

7.3.3 Multi-omics factor analysis

7.4 PRS inhibition general discussion

8

Epigenetic reversal of drug resistance in MM

8.1 Introduction

8.1.1 Experiment overviews

8.2 Dose response curves

8.3 Bulk RNA-seq

8.4 Single-cell RNA-seq

8.5 Proteomics

8.5.1 CyTOF

8.5.2 Total proteomics (LC-MS/MS)

8.5.3 Phosphoproteomics

8.5.4 Ubiquitinomics

8.6 ATAC-seq

8.7 Multi-omics factor analysis

8.8 TRIM24i general discussion

Appendices

A

Epigenetic compound screen

A compound screen consisting of approximately 140 epigenetic inhibitors was performed for AMO-1 cells.

References

- [1] Katrin Roth et al. “Tracking plasma cell differentiation and survival”. In: *Cytometry Part A* 85.1 (2014), pp. 15–24.
- [2] Michel Jourdan et al. “Characterization of a transitional preplasmablast population in the process of human B cell to plasma cell differentiation”. In: *The Journal of Immunology* 187.8 (2011), pp. 3931–3941.
- [3] Miriam Shapiro-Shelef and Kathryn Calame. “Plasma cell differentiation and multiple myeloma”. In: *Current opinion in immunology* 16.2 (2004), pp. 226–234.
- [4] Alexandra Bortnick and David Allman. “What Is and What Should Always Have Been: Long-Lived Plasma Cells Induced by T Cell–Independent Antigens”. In: *The Journal of Immunology* 190.12 (2013), pp. 5913–5918.
- [5] Mathieu Andraud et al. “Living on three time scales: the dynamics of plasma cell and antibody populations illustrated for hepatitis a virus”. In: *PLoS Comput Biol* 8.3 (2012), e1002418.
- [6] Kenneth C Anderson and Ruben D Carrasco. “Pathogenesis of myeloma”. In: *Annual Review of Pathology: Mechanisms of Disease* 6 (2011), pp. 249–274.
- [7] International Myeloma Working Group. “Criteria for the classification of monoclonal gammopathies, multiple myeloma and related disorders: a report of the International Myeloma Working Group”. In: *British journal of haematology* 121.5 (2003), pp. 749–757.
- [8] Matthew Tsang et al. “Multiple myeloma epidemiology and patient geographic distribution in Canada: a population study”. In: *Cancer* (2019).
- [9] Antonio Palumbo and Kenneth Anderson. “Multiple Myeloma”. In: *New England Journal of Medicine* 364.11 (2011), pp. 1046–1060.
- [10] NHS UK. *Multiple Myeloma*.
<https://www.nhs.uk/conditions/multiple-myeloma/>. Accessed: 06-2019.
- [11] Lauren R Teras et al. “2016 US lymphoid malignancy statistics by World Health Organization subtypes”. In: *CA: a cancer journal for clinicians* 66.6 (2016), pp. 443–459.
- [12] Andrew J Cowan et al. “Global burden of multiple myeloma: a systematic analysis for the Global Burden of Disease Study 2016”. In: *JAMA oncology* 4.9 (2018), pp. 1221–1227.
- [13] Cancer Research UK. *Myeloma Survival Statistics*.
<https://www.cancerresearchuk.org/health-professional/cancer-statistics/statistics-by-cancer-type/myeloma/survival>. Accessed: 06-2019.

- [14] Rebecca L Siegel, Kimberly D Miller, and Ahmedin Jemal. "Cancer statistics, 2016". In: *CA: a cancer journal for clinicians* 66.1 (2016), pp. 7–30.
- [15] Niels van Nieuwenhuijzen et al. "From MGUS to multiple myeloma, a paradigm for clonal evolution of premalignant cells". In: *Cancer research* 78.10 (2018), pp. 2449–2456.
- [16] S Vincent Rajkumar, Ola Landgren, and Maria-Victoria Mateos. "Smoldering multiple myeloma". In: *Blood, The Journal of the American Society of Hematology* 125.20 (2015), pp. 3069–3075.
- [17] Neha Korde, Sigurdur Y Kristinsson, and Ola Landgren. "Monoclonal gammopathy of undetermined significance (MGUS) and smoldering multiple myeloma (SMM): novel biological insights and development of early treatment strategies". In: *Blood* 117.21 (2011), pp. 5573–5581.
- [18] Robert A Kyle et al. "Clinical course and prognosis of smoldering (asymptomatic) multiple myeloma". In: *New England Journal of Medicine* 356.25 (2007), pp. 2582–2590.
- [19] S Vincent Rajkumar et al. "International Myeloma Working Group updated criteria for the diagnosis of multiple myeloma". In: *The lancet oncology* 15.12 (2014), e538–e548.
- [20] Dickran Kazandjian and Ola Landgren. "A look backward and forward in the regulatory and treatment history of multiple myeloma: approval of novel-novel agents, new drug development, and longer patient survival". In: *Seminars in oncology*. Vol. 43. 6. Elsevier. 2016, pp. 682–689.
- [21] N Blokhin et al. "Clinical experiences with sarcolysin in neoplastic diseases". In: *Annals of the New York Academy of Sciences* 68.3 (1958), pp. 1128–1132.
- [22] ROBERT E MASS. "A comparison of the effect of prednisone and a placebo in the treatment of multiple myeloma." In: *Cancer chemotherapy reports* 16 (1962), p. 257.
- [23] Raymond Alexanian et al. "Treatment for multiple myeloma: combination chemotherapy with different melphalan dose regimens". In: *Jama* 208.9 (1969), pp. 1680–1685.
- [24] TJ McElwain and RL Powles. "High-dose intravenous melphalan for plasma-cell leukaemia and myeloma". In: *The Lancet* 322.8354 (1983), pp. 822–824.
- [25] Elliott F Osserman et al. "Identical twin marrow transplantation in multiple myeloma". In: *Acta haematologica* 68.3 (1982), pp. 215–223.
- [26] Alexander Fefer, Martin A Cheever, and Philip D Greenberg. "Identical-twin (syngeneic) marrow transplantation for hematologic cancers". In: *Journal of the National Cancer Institute* 76.6 (1986), pp. 1269–1273.
- [27] G Gahrton et al. "Bone marrow transplantation in multiple myeloma: report from the European Cooperative Group for Bone Marrow Transplantation". In: *Blood* 69.4 (1987), pp. 1262–1264.
- [28] Robert C Kane et al. "Velcade®: US FDA approval for the treatment of multiple myeloma progressing on prior therapy". In: *The oncologist* 8.6 (2003), pp. 508–513.
- [29] Paul G Richardson et al. "A phase 2 study of bortezomib in relapsed, refractory myeloma". In: *New England Journal of Medicine* 348.26 (2003), pp. 2609–2617.

- [30] Alla Katsnelson. *Next-generation proteasome inhibitor approved in multiple myeloma*. 2012.
- [31] Seema Singhal et al. “Antitumor activity of thalidomide in refractory multiple myeloma”. In: *New England Journal of Medicine* 341.21 (1999), pp. 1565–1571.
- [32] FDA Label. “Revlimid-lenalidomide capsule”. In: *For Multiple Myeloma Myelodysplastic Syndrome and Mantle Cell Lymphoma* 47 () .
- [33] Jesus San Miguel et al. “Pomalidomide plus low-dose dexamethasone versus high-dose dexamethasone alone for patients with relapsed and refractory multiple myeloma (MM-003): a randomised, open-label, phase 3 trial”. In: *The lancet oncology* 14.11 (2013), pp. 1055–1066.
- [34] Henk M Lokhorst et al. “Targeting CD38 with daratumumab monotherapy in multiple myeloma”. In: *New England Journal of Medicine* 373.13 (2015), pp. 1207–1219.
- [35] Sagar Lonial et al. “Elotuzumab therapy for relapsed or refractory multiple myeloma”. In: *New England Journal of Medicine* 373.7 (2015), pp. 621–631.
- [36] Jesús F San Miguel et al. “Bortezomib plus melphalan and prednisone for initial treatment of multiple myeloma”. In: *New England Journal of Medicine* 359.9 (2008), pp. 906–917.
- [37] Philippe Moreau et al. “Proteasome inhibitors in multiple myeloma: 10 years later”. In: *Blood* 120.5 (2012), pp. 947–959.
- [38] Gary Kleiger and Thibault Mayor. “Perilous journey: a tour of the ubiquitin–proteasome system”. In: *Trends in cell biology* 24.6 (2014), pp. 352–359.
- [39] Bruce Alberts et al. *Molecular biology of the cell*. 6th ed. Garland science, Dec. 2014, pp. 356–359.
- [40] A Annunziato. “DNA packaging: nucleosomes and chromatin”. In: *Nature Education* 1.1 (2008), p. 26.
- [41] Bruce Alberts et al. “Chromosomal DNA and its packaging in the chromatin fiber”. In: *Molecular Biology of the Cell. 4th edition*. Garland science, 2002.
- [42] Fuchou Tang et al. “mRNA-Seq whole-transcriptome analysis of a single cell”. In: *Nature methods* 6.5 (2009), pp. 377–382.
- [43] Simone Picelli et al. “Smart-seq2 for sensitive full-length transcriptome profiling in single cells”. In: *Nature methods* 10.11 (2013), pp. 1096–1098.
- [44] Evan Z Macosko et al. “Highly parallel genome-wide expression profiling of individual cells using nanoliter droplets”. In: *Cell* 161.5 (2015), pp. 1202–1214.
- [45] Saiful Islam et al. “Characterization of the single-cell transcriptional landscape by highly multiplex RNA-seq”. In: *Genome research* 21.7 (2011), pp. 1160–1167.
- [46] Allon M Klein et al. “Droplet barcoding for single-cell transcriptomics applied to embryonic stem cells”. In: *Cell* 161.5 (2015), pp. 1187–1201.
- [47] Lluis Ribas de Pouplana. “The evolution of aminoacyl-tRNA synthetases: From dawn to LUCA”. In: *Biology of Aminoacyl-tRNA Synthetases* 48 (2020), p. 11.
- [48] Kate J Newberry, Ya-Ming Hou, and John J Perona. “Structural origins of amino acid selection without editing by cysteinyl-tRNA synthetase”. In: *The EMBO Journal* 21.11 (2002), pp. 2778–2787.

- [49] Nam Hoon Kwon, Paul L Fox, and Sunghoon Kim. “Aminoacyl-tRNA synthetases as therapeutic targets”. In: *Nature reviews Drug discovery* 18.8 (2019), pp. 629–650.
- [50] L Pauling. *Festschrift für Prof. Dr. Arthur Stoll*. 1958.
- [51] ROBERT B Loftfield and DOROTHY Vanderjagt. “The frequency of errors in protein biosynthesis.” In: *Biochemical Journal* 128.5 (1972), p. 1353.
- [52] Jeong Woong Lee et al. “Editing-defective tRNA synthetase causes protein misfolding and neurodegeneration”. In: *Nature* 443.7107 (2006), pp. 50–55.
- [53] Jong Hyun Kim et al. “Evolution of the multi-tRNA synthetase complex and its role in cancer”. In: *Journal of Biological Chemistry* 294.14 (2019), pp. 5340–5351.
- [54] Krishnendu Khan et al. “3-Dimensional architecture of the human multi-tRNA synthetase complex”. In: *Nucleic acids research* 48.15 (2020), pp. 8740–8754.
- [55] Myung Hee Kim and Sunghoon Kim. “Structures and functions of multi-tRNA synthetase complexes”. In: *Biology of Aminoacyl-tRNA Synthetases* 48 (2020), p. 149.
- [56] Ha Yeon Cho et al. “Assembly of multi-tRNA synthetase complex via heterotetrameric glutathione transferase-homology domains”. In: *Journal of Biological Chemistry* 290.49 (2015), pp. 29313–29328.
- [57] Monika Kaminska et al. “Dissection of the structural organization of the aminoacyl-tRNA synthetase complex”. In: *Journal of Biological Chemistry* 284.10 (2009), pp. 6053–6060.
- [58] Marc Mirande. “The aminoacyl-tRNA synthetase complex”. In: *Macromolecular Protein Complexes* (2017), pp. 505–522.
- [59] Jung Min Han et al. “Hierarchical network between the components of the multi-tRNA synthetase complex: implications for complex formation”. In: *Journal of Biological Chemistry* 281.50 (2006), pp. 38663–38667.
- [60] Jung Min Han et al. “Leucyl-tRNA synthetase is an intracellular leucine sensor for the mTORC1-signaling pathway”. In: *Cell* 149.2 (2012), pp. 410–424.
- [61] Nurit Yannay-Cohen et al. “LysRS serves as a key signaling molecule in the immune response by regulating gene expression”. In: *Molecular cell* 34.5 (2009), pp. 603–611.
- [62] Abul Arif et al. “Two-site phosphorylation of EPRS coordinates multimodal regulation of noncanonical translational control activity”. In: *Molecular cell* 35.2 (2009), pp. 164–180.
- [63] Abul Arif et al. “The GAIT translational control system”. In: *Wiley Interdisciplinary Reviews: RNA* 9.2 (2018), e1441.
- [64] Sang Gyu Park et al. “Precursor of pro-apoptotic cytokine modulates aminoacylation activity of tRNA synthetase”. In: *Journal of Biological Chemistry* 274.24 (1999), pp. 16673–16676.
- [65] Sang Gyu Park et al. “Hormonal activity of AIMP1/p43 for glucose homeostasis”. In: *Proceedings of the National Academy of Sciences* 103.40 (2006), pp. 14913–14918.

- [66] Zheng Zhou et al. “Roles of aminoacyl-tRNA synthetase-interacting multi-functional proteins in physiology and cancer”. In: *Cell Death & Disease* 11.7 (2020), pp. 1–14.
- [67] Nam Hoon Kwon et al. “Dual role of methionyl-tRNA synthetase in the regulation of translation and tumor suppressor activity of aminoacyl-tRNA synthetase-interacting multifunctional protein-3”. In: *Proceedings of the National Academy of Sciences* 108.49 (2011), pp. 19635–19640.
- [68] Peng Yao and Paul L Fox. “Aminoacyl-tRNA synthetases in medicine and disease”. In: *EMBO molecular medicine* 5.3 (2013), pp. 332–343.
- [69] Sven Bervoets et al. “Transcriptional dysregulation by a nucleus-localized aminoacyl-tRNA synthetase associated with Charcot-Marie-Tooth neuropathy”. In: *Nature communications* 10.1 (2019), pp. 1–14.
- [70] Anzheng Nie et al. “Roles of aminoacyl-tRNA synthetases in immune regulation and immune diseases”. In: *Cell death & disease* 10.12 (2019), pp. 1–14.
- [71] Eun-Young Lee et al. “Infection-specific phosphorylation of glutamyl-prolyl tRNA synthetase induces antiviral immunity”. In: *Nature immunology* 17.11 (2016), pp. 1252–1262.
- [72] Alice A Duchon et al. “HIV-1 exploits a dynamic multi-aminoacyl-tRNA synthetase complex to enhance viral replication”. In: *Journal of virology* 91.21 (2017), e01240–17.
- [73] Young Ha Ahn et al. “Secreted tryptophanyl-tRNA synthetase as a primary defence system against infection”. In: *Nature microbiology* 2.1 (2016), pp. 1–13.
- [74] Zhongying Mo et al. “Neddylation requires glycyl-tRNA synthetase to protect activated E2”. In: *Nature structural & molecular biology* 23.8 (2016), pp. 730–737.
- [75] Lu Deng et al. “The role of ubiquitination in tumorigenesis and targeted drug discovery”. In: *Signal transduction and targeted therapy* 5.1 (2020), pp. 1–28.
- [76] Nam Hoon Kwon et al. “Stabilization of cyclin-dependent kinase 4 by methionyl-tRNA synthetase in p16INK4a-negative cancer”. In: *ACS pharmacology & translational science* 1.1 (2018), pp. 21–31.
- [77] Tamara F Williams et al. “Secreted Threonyl-tRNA synthetase stimulates endothelial cell migration and angiogenesis”. In: *Scientific reports* 3.1 (2013), pp. 1–7.
- [78] Adam C Mirando et al. “Aminoacyl-tRNA synthetase dependent angiogenesis revealed by a bioengineered macrolide inhibitor”. In: *Scientific reports* 5.1 (2015), pp. 1–17.
- [79] Cindy Mendes et al. “Unraveling FATP1, regulated by ER- β , as a targeted breast cancer innovative therapy”. In: *Scientific reports* 9.1 (2019), pp. 1–15.
- [80] Jin Woo Choi et al. “Multidirectional tumor-suppressive activity of AIMP2/p38 and the enhanced susceptibility of AIMP2 heterozygous mice to carcinogenesis”. In: *Carcinogenesis* 30.9 (2009), pp. 1638–1644.
- [81] Jung Min Han, Heejoon Myung, and Sunghoon Kim. “Antitumor activity and pharmacokinetic properties of ARS-interacting multi-functional protein 1 (AIMP1/p43)”. In: *Cancer letters* 287.2 (2010), pp. 157–164.

- [82] Yeon-Sook Lee et al. "Antitumor activity of the novel human cytokine AIMP1 in an in vivo tumor model." In: *Molecules & Cells (Springer Science & Business Media BV)* 21.2 (2006).
- [83] Sang Gyu Park et al. "Dose-dependent biphasic activity of tRNA synthetase-associating factor, p43, in angiogenesis". In: *Journal of Biological Chemistry* 277.47 (2002), pp. 45243–45248.
- [84] Myun Soo Kim et al. "Aminoacyl tRNA synthetase-interacting multifunctional protein 1 activates NK cells via macrophages in vitro and in vivo". In: *The Journal of Immunology* 198.10 (2017), pp. 4140–4147.
- [85] Bum-Joon Park et al. "The haploinsufficient tumor suppressor p18 upregulates p53 via interactions with ATM/ATR". In: *Cell* 120.2 (2005), pp. 209–221.
- [86] Julian Gregston Hurdle, Alexander John O'Neill, and Ian Chopra. "Prospects for aminoacyl-tRNA synthetase inhibitors as new antimicrobial agents". In: *Antimicrobial agents and chemotherapy* 49.12 (2005), pp. 4821–4833.
- [87] Julia Hughes and Graham Mellows. "Interaction of pseudomonic acid A with Escherichia coli B isoleucyl-tRNA synthetase". In: *Biochemical Journal* 191.1 (1980), pp. 209–219.
- [88] Takashi Nakama, Osamu Nureki, and Shigeyuki Yokoyama. "Structural basis for the recognition of isoleucyl-adenylate and an antibiotic, mupirocin, by isoleucyl-tRNA synthetase". In: *Journal of Biological Chemistry* 276.50 (2001), pp. 47387–47393.
- [89] James S Pham et al. "Aminoacyl-tRNA synthetases as drug targets in eukaryotic parasites". In: *International Journal for Parasitology: Drugs and Drug Resistance* 4.1 (2014), pp. 1–13.
- [90] JB Koepfli, JF Mead, and John A Brockman. "Alkaloids of Dichroa febrifuga. I. Isolation and degradative studies". In: *Journal of the American Chemical Society* 71.3 (1949), pp. 1048–1054.
- [91] Sharon Mordechay et al. "Differential Effects of Halofuginone Enantiomers on Muscle Fibrosis and Histopathology in Duchenne Muscular Dystrophy". In: *International Journal of Molecular Sciences* 22.13 (2021), p. 7063.
- [92] Michael R Linder et al. "(2R, 3S)-(+)-and (2S, 3R)-(-)-Halofuginone lactate: Synthesis, absolute configuration, and activity against Cryptosporidium parvum". In: *Bioorganic & medicinal chemistry letters* 17.15 (2007), pp. 4140–4143.
- [93] European Organisation for Research and Treatment of Cancer - EORTC. *Halofuginone Hydrobromide in Treating Patients With Progressive Advanced Solid Tumors*. Accessed: 2021-10-27. 2012.
- [94] National Cancer Institute (NCI). *Halofuginone Hydrobromide in Treating Patients With HIV-Related Kaposi's Sarcoma*. Accessed: 2021-10-27. 2013.
- [95] Mark S Sundrud et al. "Halofuginone inhibits TH17 cell differentiation by activating the amino acid starvation response". In: *Science* 324.5932 (2009), pp. 1334–1338.
- [96] Tracy L Keller et al. "Halofuginone and other febrifugine derivatives inhibit prolyl-tRNA synthetase". In: *Nature chemical biology* 8.3 (2012), pp. 311–317.

- [97] Huihao Zhou et al. “ATP-directed capture of bioactive herbal-based medicine on human tRNA synthetase”. In: *Nature* 494.7435 (2013), pp. 121–124.
- [98] Jiangbin Ye et al. “GCN2 sustains mTORC1 suppression upon amino acid deprivation by inducing Sestrin2”. In: *Genes & development* 29.22 (2015), pp. 2331–2336.
- [99] Rinat Abramovitch et al. “Halofuginone inhibits angiogenesis and growth in implanted metastatic rat brain tumor model—an MRI study”. In: *Neoplasia* 6.5 (2004), pp. 480–489.
- [100] Michael Elkin et al. “Inhibition of bladder carcinoma angiogenesis, stromal support, and tumor growth by halofuginone”. In: *Cancer research* 59.16 (1999), pp. 4111–4118.
- [101] Zohar Gavish et al. “Growth inhibition of prostate cancer xenografts by halofuginone”. In: *The Prostate* 51.2 (2002), pp. 73–83.
- [102] Olga Genin et al. “Myofibroblasts in pulmonary and brain metastases of alveolar soft-part sarcoma: a novel target for treatment?” In: *Neoplasia* 10.9 (2008), pp. 940–948.
- [103] David J Gross et al. “Treatment with halofuginone results in marked growth inhibition of a von Hippel-Lindau pheochromocytoma in vivo”. In: *Clinical cancer research* 9.10 (2003), pp. 3788–3793.
- [104] Arnon Nagler et al. “Suppression of hepatocellular carcinoma growth in mice by the alkaloid coccidiostat halofuginone”. In: *European Journal of Cancer* 40.9 (2004), pp. 1397–1403.
- [105] Yaqiu Wang, Zhihui Xie, and Hong Lu. “Significance of halofuginone in esophageal squamous carcinoma cell apoptosis through HIF-1 α -FOXO3a pathway”. In: *Life Sciences* 257 (2020), p. 118104.
- [106] Asuman Demiroglu-Zergeroglu et al. “Anticarcinogenic effects of halofuginone on lung-derived cancer cells”. In: *Cell Biology International* 44.9 (2020), pp. 1934–1944.
- [107] Xiaojing Xia et al. “Halofuginone-induced autophagy suppresses the migration and invasion of MCF-7 cells via regulation of STMN1 and p53”. In: *Journal of cellular biochemistry* 119.5 (2018), pp. 4009–4020.
- [108] Henry B Koon et al. “PHASE II AIDS MALIGNANCY CONSORTIUM TRIAL OF TOPICAL HALOFUGINONE IN AIDS-RELATED KAPOSI’S SARCOMA”. In: *Journal of acquired immune deficiency syndromes* (1999) 56.1 (2011), p. 64.
- [109] Merav Leiba et al. “Halofuginone inhibits multiple myeloma growth in vitro and in vivo and enhances cytotoxicity of conventional and novel agents”. In: *British journal of haematology* 157.6 (2012), pp. 718–731.
- [110] GP Soriano et al. “Proteasome inhibitor-adapted myeloma cells are largely independent from proteasome activity and show complex proteomic changes, in particular in redox and energy metabolism”. In: *Leukemia* 30.11 (2016), pp. 2198–2207.
- [111] David Sims et al. “CGAT: computational genomics analysis toolkit”. In: *Bioinformatics* 30.9 (2014), pp. 1290–1291.

- [112] Nicolas L Bray et al. “Near-optimal probabilistic RNA-seq quantification”. In: *Nature biotechnology* 34.5 (2016), p. 525.
- [113] Michael I Love, Wolfgang Huber, and Simon Anders. “Moderated estimation of fold change and dispersion for RNA-seq data with DESeq2”. In: *Genome biology* 15.12 (2014), p. 550.
- [114] Hai Fang et al. “XGR software for enhanced interpretation of genomic summary data, illustrated by application to immunological traits”. In: *Genome medicine* 8.1 (2016), pp. 1–20.
- [115] Antonio Fabregat et al. “Reactome pathway analysis: a high-performance in-memory approach”. In: *BMC bioinformatics* 18.1 (2017), p. 142.
- [116] Minoru Kanehisa et al. “KEGG: new perspectives on genomes, pathways, diseases and drugs”. In: *Nucleic acids research* 45.D1 (2017), pp. D353–D361.
- [117] M Carlson. *org. Hs. eg. db: Genome Wide Annotation for Human. R package version 3.2.* 3. 2019.
- [118] H Pagès et al. “AnnotationDbi: Manipulation of SQLite-based annotations in Bioconductor”. In: *Bioconductor version: Release (3.10)* (2020).
- [119] Steffen Durinck et al. “Mapping identifiers for the integration of genomic datasets with the R/Bioconductor package biomaRt”. In: *Nature protocols* 4.8 (2009), p. 1184.
- [120] Yong Zhang et al. “Model-based analysis of ChIP-Seq (MACS)”. In: *Genome biology* 9.9 (2008), pp. 1–9.
- [121] Johannes Köster and Sven Rahmann. “Snakemake—a scalable bioinformatics workflow engine”. In: *Bioinformatics* 28.19 (2012), pp. 2520–2522.
- [122] Leo Goodstadt. “Ruffus: a lightweight Python library for computational pipelines”. In: *Bioinformatics* 26.21 (2010), pp. 2778–2779.
- [123] Adam P Cribbs et al. “CGAT-core: a python framework for building scalable, reproducible computational biology workflows”. In: *F1000Research* 8 (2019).
- [124] Cole Trapnell, Lior Pachter, and Steven L Salzberg. “TopHat: discovering splice junctions with RNA-Seq”. In: *Bioinformatics* 25.9 (2009), pp. 1105–1111.
- [125] Alexander Dobin et al. “STAR: ultrafast universal RNA-seq aligner”. In: *Bioinformatics* 29.1 (2013), pp. 15–21.
- [126] Ali Mortazavi et al. “Mapping and quantifying mammalian transcriptomes by RNA-Seq”. In: *Nature methods* 5.7 (2008), p. 621.
- [127] Marius Nicolae et al. “Estimation of alternative splicing isoform frequencies from RNA-Seq data”. In: *International Workshop on Algorithms in Bioinformatics*. Springer. 2010, pp. 202–214.
- [128] Rob Patro et al. “Salmon provides fast and bias-aware quantification of transcript expression”. In: *Nature methods* 14.4 (2017), p. 417.
- [129] Pál Melsted, Vasilis Ntranos, and Lior Pachter. “The barcode, UMI, set format and BUStools”. In: *bioRxiv* (2018), p. 472571.
- [130] Pál Melsted et al. “Modular and efficient pre-processing of single-cell RNA-seq”. In: *BioRxiv* (2019), p. 673285.

- [131] Avi Srivastava et al. “Alevin efficiently estimates accurate gene abundances from dscRNA-seq data”. In: *Genome biology* 20.1 (2019), p. 65.
- [132] Davis J McCarthy et al. “Scater: pre-processing, quality control, normalization and visualization of single-cell RNA-seq data in R”. In: *Bioinformatics* 33.8 (2017), pp. 1179–1186.
- [133] Tim Stuart et al. “Comprehensive Integration of Single-Cell Data”. In: *Cell* (2019).
- [134] Cole Trapnell et al. “The dynamics and regulators of cell fate decisions are revealed by pseudotemporal ordering of single cells”. In: *Nature biotechnology* 32.4 (2014), p. 381.
- [135] Gioele La Manno et al. “RNA velocity of single cells”. In: *Nature* 560.7719 (2018), p. 494.
- [136] S Manier et al. “Bone marrow microenvironment in multiple myeloma progression”. In: *Journal of Biomedicine and Biotechnology* 2012 (2012).
- [137] Yawara Kawano et al. “Targeting the bone marrow microenvironment in multiple myeloma”. In: *Immunological reviews* 263.1 (2015), pp. 160–172.
- [138] David Melnekoff et al. “Single-cell RNA sequencing reveals distinct transcriptomic profiles of multiple myeloma with implications for personalized medicine”. In: *Blood* 130.Supplement 1 (2017), pp. 62–62.
- [139] Guy Ledergor et al. “Single cell dissection of plasma cell heterogeneity in symptomatic and asymptomatic myeloma”. In: *Nature medicine* 24.12 (2018), pp. 1867–1876.